Neuron

Article

Single-cell spatial transcriptomic atlas of the whole mouse brain

Graphical abstract

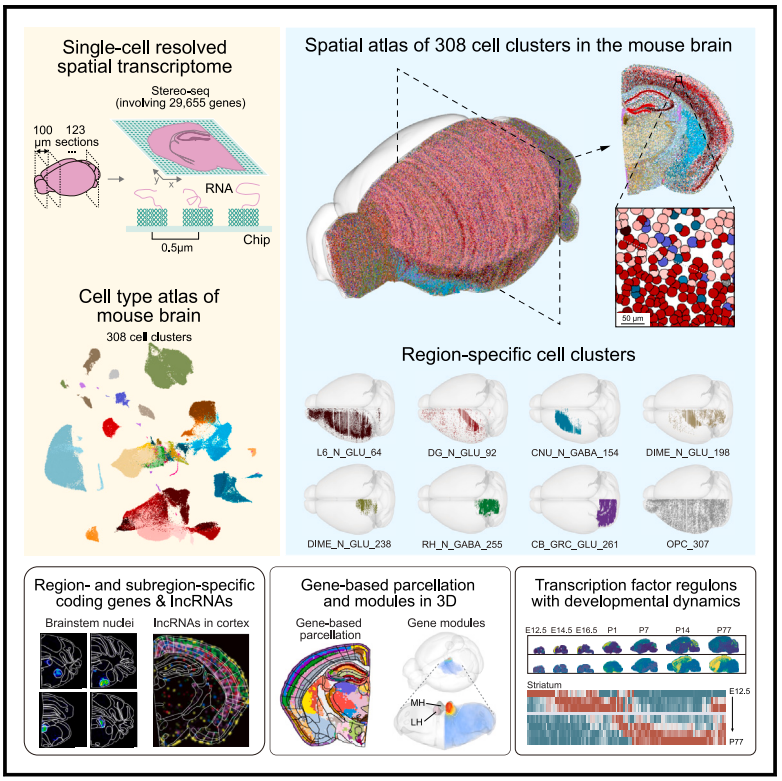

Highlights

- A whole-transcriptome spatial atlas of the mouse brain at single-cell resolution
- Revealed region- and subregion-enriched coding genes and lncRNAs
- Gene-based parcellation reveals fine structural organization of multiple brain areas
- Transcription factor regulons exhibit spatiotemporal dynamics in developing mouse brain

Authors

Lei Han, Zhen Liu, Zehua Jing, ..., Zhiming Shen, Wu Wei, Yan-Gang Sun

Correspondence

xfwang@ion.ac.cn (X.W.), lichao0015@ion.ac.cn (C.L.), jianhuayao@tencent.com (J.Y.), xuxun@genomics.cn (X.X.), liulongqi@genomics.cn (L.L.), zmshen@ion.ac.cn (Z.S.), wuwei@lglab.ac.cn (W.W.), yangang.sun@ion.ac.cn (Y.-G.S.)

In brief

Han et al. used snRNA-seq and Stereo-seq to generate a detailed mouse brain atlas with over 4 million spatially resolved cells and 29,655 genes. Their findings include region- enriched cell clusters and genes, spatiotemporal dynamics of transcription factor regulons, and a gene-based parcellation framework, providing a comprehensive resource for brain architecture.

Han et al., 2025, Neuron *113*, 1–20
July 9, 2025
https://doi.org/10.1016/j.neuron.2025.02.015

CellPress

Please cite this article in press as: Han et al., Single-cell spatial transcriptomic atlas of the whole mouse brain, Neuron (2025), https://doi.org/10.1016/j.neuron.2025.02.015

Neuron

CellPress

Article

Single-cell spatial transcriptomic atlas of the whole mouse brain

Lei Han,[1,24] Zhen Liu,[2,3,24] Zehua Jing,[1,4,24] Yuxuan Liu,[3,24] Yujie Peng,[1,24] Huizhong Chang,[1,24] Junjie Lei,[1,4,24] Kexin Wang,[5,24] Yuanfang Xu,[5,24] Wei Liu,[2,24] Zihan Wu,[6,24] Qian Li,[4,7] Xiaoxue Shi,[5] Mingyuan Zheng,[5] He Wang,[5] Juan Deng,[8] Yanqing Zhong,[5] Hailin Pan,[7] Junkai Lin,[5] Ruiyi Zhang,[5] Yu Chen,[5] Jinhua Wu,[2] Mingrui Xu,[9] Biyu Ren,[5] Mengnan Cheng,[1] Qian Yu,[5] Xinxiang Song,[5] Yanbing Lu,[5] Yuanchun Tang,[1,10] Nini Yuan,[5] Suhong Sun,[5] Yingjie An,[5] Wenqun Ding,[5] Xing Sun,[2,5] Yanrong Wei,[1,4] Shuzhen Zhang,[5] Yannong Dou,[5] Yun Zhao,[5] Luyao Han,[5] Qianhua Zhu,[7] Junfeng Xu,[5] Shiwen Wang,[5] Dan Wang,[5] Yinqi Bai,[1] Yikai Liang,[5] Yuan Liu,[5] Mengni Chen,[5] Chun Xie,[5] Binshi Bo,[5]

(Author list continued on next page)

[1]BGI Research, Hangzhou 310030, China
[2]Lingang Laboratory, Shanghai 200031, China
[3]CAS Key Laboratory of Computational Biology, Shanghai Institute of Nutrition and Health, University of Chinese Academy of Sciences, Chinese Academy of Sciences, Shanghai 200031, China
[4]College of Life Sciences, University of Chinese Academy of Sciences, Beijing 100049, China
[5]Institute of Neuroscience, State Key Laboratory of Brain Cognition and Brain-inspired Intelligence Technology, CAS Center for Excellence in Brain Science and Intelligence Technology, University of Chinese Academy of Sciences, Chinese Academy of Sciences, Shanghai 200031, China
[6]Tencent AI Lab, Shenzhen 518057, China
[7]BGI Research, Shenzhen 518083, China
[8]Department of Anesthesiology, Huashan Hospital, State Key Laboratory of Medical Neurobiology, Institute for Translational Brain Research, MOE Frontiers Center for Brain Science, Fudan University, Shanghai 200032, China
[9]State Key Laboratory of Molecular Development Biology, Institute of Genetics and Developmental Biology, Chinese Academy of Sciences, Beijing 100101, China
[10]BGI College & Henan Institute of Medical and Pharmaceutical Sciences, Zhengzhou University, Zhengzhou 450000, China
[11]School of Biology and Biological Engineering, South China University of Technology, Guangzhou 510006, China
[12]BGI Research, Qingdao 266555, China
[13]China National GeneBank, BGI Research, Shenzhen 518120, China
[14]Shenzhen Proof-of-Concept Center of Digital Cytopathology, BGI Research, Shenzhen 518083, China

(Affiliations continued on next page)

SUMMARY

A comprehensive atlas of genes, cell types, and their spatial distribution across a whole mammalian brain is fundamental for understanding the function of the brain. Here, using single-nucleus RNA sequencing (snRNA-seq) and Stereo-seq techniques, we generated a mouse brain atlas with spatial information for 308 cell clusters at single-cell resolution, involving over 4 million cells, as well as for 29,655 genes. We have identified cell clusters exhibiting preference for cortical subregions and explored their associations with brain-related diseases. Additionally, we pinpointed 155 genes with distinct regional expression patterns within the brainstem and unveiled 513 long non-coding RNAs showing region-enriched expression in the adult brain. Parcellation of brain regions based on spatial transcriptomic information revealed fine structure for several brain areas. Furthermore, we have uncovered 411 transcription factor regulons showing distinct spatiotemporal dynamics during neurodevelopment. Thus, we have constructed a single-cell-resolution spatial transcriptomic atlas of the mouse brain with genome-wide coverage.

INTRODUCTION

The complexity of mammalian brains, characterized by diverse cell types and their specific distribution and connectivity, poses a significant challenge to understanding the neural circuits underlying behavior. Extensive efforts have been made to construct brain atlases for the mouse, the most widely used animal model. These include anatomical atlases based on traditional cytoarchitectural features,[1] a gene expression atlas covering ~20,000 genes,[2] and a single-cell transcriptome atlas

Please cite this article in press as: Han et al., Single-cell spatial transcriptomic atlas of the whole mouse brain, Neuron (2025), https://doi.org/10.1016/j.neuron.2025.02.015

Mei Li,[7] Xinyan Zhang,[5] Wang Ting,[9] Zhenhua Chen,[9] Jiao Fang,[5] Shuting Li,[5] Yujia Jiang,[1] Xing Tan,[5] Guolong Zuo,[5] Yue Xie,[7] Huanhuan Li,[5] Quyuan Tao,[1,4] Yan Li,[5] Jianfeng Liu,[5] Yuyang Liu,[1,4] Mingkun Hao,[2,5] Jingjing Wang,[9] Huiying Wen,[1,11] Jiabing Liu,[5] Yizhen Yan,[7] Hui Zhang,[5] Yifan Sheng,[2,5] Shui Yu,[5] Xiaoyan Liao,[7] Xuyin Jiang,[5] Guangling Wang,[5] Huanlin Liu,[7] Congcong Wang,[2,5] Ning Feng,[7] Xin Liu,[5] Kailong Ma,[7] Xiangjie Xu,[5] Tianyue Han,[7] Huateng Cao,[5] Huiwen Zheng,[1,4] Yadong Chen,[12] Haorong Lu,[13] Zixian Yu,[5] Jinsong Zhang,[12] Bo Wang,[13] Zhifeng Wang,[7] Qing Xie,[7] Shanshan Pan,[12] Chuanyu Liu,[7,14,15] Chan Xu,[12] Luman Cui,[7] Yuxiang Li,[7,16] Shiping Liu,[1,7] Sha Liao,[7,17,18] Ao Chen,[7,17,18,19] Qing-Feng Wu,[9] Jian Wang,[7,13] Zhiyong Liu,[5,20] Yidi Sun,[5] Jan Mulder,[21,22] Huanming Yang,[7] Xiaofei Wang,[5,*] Chao Li,[5,*] Jianhua Yao,[6,*] Xun Xu,[7,15,23,*] Longqi Liu,[1,7,15,*] Zhiming Shen,[5,20,*] Wu Wei,[2,3,*] and Yan-Gang Sun[5,25,*]

[15]Shanxi Medical University-BGI Collaborative Center for Future Medicine, Shanxi Medical University, Taiyuan 030001, China
[16]BGI Research, Wuhan 430074, China
[17]BGI Research, Chongqing 401329, China
[18]JFL-BGI STOmics Center, Jinfeng Laboratory, Chongqing 401329, China
[19]Department of Biology, University of Copenhagen, Copenhagen 2200, Denmark
[20]Shanghai Center for Brain Science and Brain-Inspired Technology, Shanghai 201602, China
[21]Department of Protein Science, Science for Life Laboratory, KTH-Royal Institute of Technology, Stockholm 17121, Sweden
[22]Department of Neuroscience, Karolinska Institute, Stockholm 17177, Sweden
[23]Guangdong Provincial Key Laboratory of Genome Read and Write, BGI Research, Shenzhen 518083, China
[24]These authors contributed equally
[25]Lead contact
*Correspondence: xfwang@ion.ac.cn (X.W.), lichao0015@ion.ac.cn (C.L.), jianhuayao@tencent.com (J.Y.), xuxun@genomics.cn (X.X.), liulongqi@genomics.cn (L.L.), zmshen@ion.ac.cn (Z.S.), wuwei@lglab.ac.cn (W.W.), yangang.sun@ion.ac.cn (Y.-G.S.)
https://doi.org/10.1016/j.neuron.2025.02.015

revealing brain-cell-type diversity.[3] However, a comprehensive brain atlas across the whole mouse brain with single-cell and high spatial resolution is still lacking.

Recent advancements in spatial transcriptomics have provided an unprecedented opportunity to map gene expression and cell types with high spatial resolution.[4] *In situ* hybridization-based (ISH) and sequencing-based (ISS) techniques, such as multiplexed error-robust fluorescence *in situ* hybridization (MERFISH)[5] and STARmap,[6] have shown high capture efficiency and spatial resolution but are limited to a small number of pre-selected genes. In contrast, spatial barcoding methods like Visium[7] and Slide-seq[8,9] offer whole-transcriptome analysis but lack single-cell resolution. Despite various efforts to construct mouse brain atlases using imaging[10–14] and sequencing-based[15–17] techniques, a comprehensive spatial map of the mouse brain, with both genome-wide coverage and single-cell resolution, is still not available.

Development of the brain is guided by genetic programs governed by a variety of specific transcription factors (TFs). Previous studies have revealed molecular heterogeneity of the mouse brain at the embryonic stage with single-cell RNA and spatial transcriptomics sequencing.[18,19] However, genes with time-dependent dynamics and gradient distribution, potentially involved in development, were not systematically examined. Spatiotemporal profiling of gene expression would be essential to reveal the genetic program driving brain development. Additionally, brain maturation continues postnatally, but the spatiotemporal gene expression profiles during these stages were not well examined. Therefore, further analysis of spatiotemporal dynamics of genes, from the embryonic to the adult stage, is essential for a comprehensive understanding of the mechanism underlying brain development.

Accumulating evidences have shown that non-coding RNAs (ncRNAs), especially long non-coding RNAs (lncRNAs), play important roles in a wide range of biological processes of the mammalian brain, including brain development, maturation, and diseases.[20,21] For example, lncRNA *Pnky* has been shown to be essential for brain development.[22] lncRNA *Evf2* can function as a *Dlx2* transcriptional coactivator and enhance the activity of *Dlx2*, which is essential for the differentiation and migration of neurons in the brain.[23] For some lncRNAs, their functional roles are highly related to their region-enriched expression pattern in the brain.[24] Although bulk sequencing studies have characterized the lncRNAs in various mouse brain regions,[25,26] a comprehensive analysis of their region-selective expression patterns and potential regulatory roles within regulons and adjacent gene pairs throughout the brain is still lacking.

Here, we applied Stereo-seq, a spatial transcriptomic technology with single-cell resolution,[19] combined with single-nucleus RNA sequencing (snRNA-seq) data to construct a 3D single-cell transcriptomic atlas that illustrated cell-type distribution across the mouse brain (https://mouse.digital-brain.cn/spatial-omics). Moreover, using data from different developmental stages, we revealed the spatiotemporal dynamics of genes, gene modules, and TF regulons. This comprehensive dataset thereby provides a valuable resource of the spatial atlas of the mouse brain, laying the foundation for studying development, function, and gene regulation of the mouse brain.

RESULTS

Spatial transcriptomic analysis of the mouse brain

We employed Stereo-seq—a sequencing-based, genome-wide, and high-resolution spatial transcriptomic technology[19]—to generate a spatial gene and cell atlas of the adult mouse brain. Coronal sections (10-μm thick) of the left hemisphere were prepared at 100-μm intervals (Figure 1A), producing 123 sections (after quality control, Figure S1; STAR Methods) with expression profiles for 29,655 genes, covering 95.5% of annotated protein-coding and non-coding genes. The distribution maps of region-specific genes by Stereo-seq were in line with ISH-based data[2] in the Allen Brain Atlas (ABA) (Figure S2A). We defined the

Please cite this article in press as: Han et al., Single-cell spatial transcriptomic atlas of the whole mouse brain, Neuron (2025), https://doi.org/10.1016/j.neuron.2025.02.015

CellPress

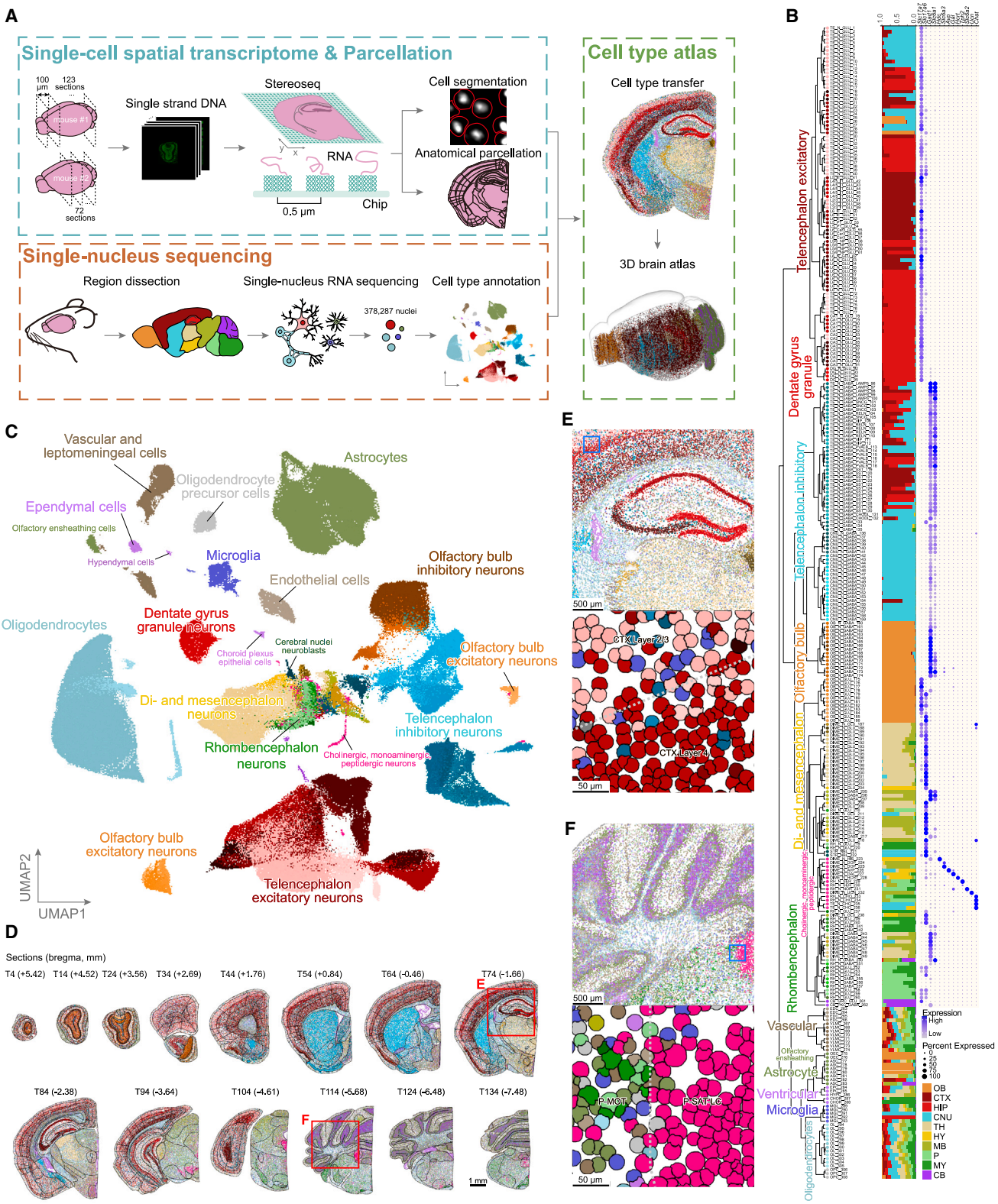

(legend on next page)

Please cite this article in press as: Han et al., Single-cell spatial transcriptomic atlas of the whole mouse brain, Neuron (2025), https://doi.org/10.1016/j.neuron.2025.02.015

boundary of each cell based on the image of single-stranded DNA (ssDNA) as described previously.[19] A total of 4,229,623 cells were characterized in one mouse brain, with an average of 1,267 molecular identifiers (MIDs) and 668 detected genes per cell (Figure S2B; Table S1). Moreover, we manually segmented the brain areas for each section based on cytoarchitectural pattern and brain region delineation in ABA common coordinate framework (CCFv3)[27] (Figure 1A).

Given the limited gene detection per cell for precise cell-type annotation, we performed snRNA-seq for all major brain regions in order to obtain a comprehensive set of cell annotation (Figure 1A; Table S1). This yielded 378,287 high-quality nuclei, classified into 6 cell classes, 19 subclasses, and 308 clusters via iterative clustering (Figures 1B and 1C; Table S2; STAR Methods). Canonical marker genes[3,5,28] refined these annotations (Figure S2C), generating 262 neuronal clusters and 46 non-neuronal clusters. Random forest analysis demonstrated robust classification accuracy of cell clusters (83.1%) (Figure S2D). In addition, we compared the cell clusters with two previously published mouse brain datasets[3,28] (Figure S2E) and found a high degree of consistency.

We next annotated spatial cells by leveraging the cell clusters defined in the snRNA-seq dataset, utilizing Spatial-ID.[29] Over 4.2 million high-quality cells were annotated (Figures S3A and S3B; STAR Methods). Spatial distribution of example cell clusters was illustrated in 14 coronal sections along the anterior-posterior axis (Figure 1D). Specific cell clusters showed distinct regional preferences, such as laminar-distributed glutamatergic neurons in the hippocampus and cortex (Figure 1E) and noradrenergic neurons in the locus coeruleus (Figure 1F).

Additionally, we demonstrated that Spatial-ID has high consistency and accuracy on Stereo-seq cell-type annotation (Figures S3C–S3F; STAR Methods). To verify reproducibility, we collected 72 coronal sections (3.2 million cells) from a second mouse brain (mouse #2, Figures 1A and S2B) and showed consistent cell-type distribution and molecular signatures between animals (Figures S3G–S3I). Moreover, we integrated the Allen whole mouse brain single-cell dataset[13] with our Stereo-seq data to evaluate the consistency of cell-type transfer across various reference datasets (Figures S4A–S4C). These results aligned with previous MERFISH-based annotations.[12]

By integrating the 123 coronal sections dataset, we constructed a comprehensive 3D atlas of cell-type distribution in the mouse brain (Figure 1A; Video S1). An interactive website was developed to facilitate exploration of specific gene and cell-type distribution (https://mouse.digital-brain.cn/spatial-omics, Figure S5).

Spatial distribution of diverse cell types in the brain

We quantitatively assessed the brain-wide distribution of 308 cell clusters across 66 parcellated brain areas in the mouse brain (Figure 2A). Most clusters, particularly neuronal clusters, exhibited clear regional preference (Figures 2A and 2B; Video S1). For cortical cells, most glutamatergic excitatory neurons exhibited both regional and layer-specific enrichment (Figure S6A). Among the glutamatergic neurons identified in snRNA-seq, 31 clusters were highly overlapped with the published dataset of the mouse cerebral cortex[28] (Figure S6B; STAR Methods) and were categorized into 8 layer-specific cortical cell groups (Figures 2C–2F). Their spatial distribution is aligned with marker gene expression (Figure S6C). Furthermore, we identified glutamatergic neurons enriched in specific cortical areas (Figures 2G, 2H, and S6D), such as one cluster (L5/6_NP_GLU_61) in the retrosplenial area (RSP) and four layer-6 clusters (L6_N_GLU_63/65/66/69) in the infralimbic area (ILA) (Figures 2H, 2I, and S6E). Differential gene expression analysis of ILA-enriched L6_N_GLU clusters versus other L6_N_GLU clusters, combined with enrichment analysis of 123 brain-disease-related gene sets,[30–32] revealed high expression of depression-associated genes in ILA-enriched clusters (Figures S6F and S6G), indicating potential involvement of ILA layer-6 neurons in mood disorders.

For GABAergic inhibitory neurons within the cortex, 37 clusters were summarized to 7 groups according to the expression of *Lamp5*, *Sncg*, *Reln*, *Vip*, *Pvalb*, *Sst*, and *Chodl* genes, marking key GABAergic neuron subtypes[28,34] (Figure S6H). Among these GABAergic neurons, Pvalb and Sst neurons were dominant in the mouse cortex (Figures S6I–S6K). Most GABAergic neurons exhibited less layer preference compared with glutamatergic neurons (Figure S6L). However, several clusters exhibited layer enrichment; for example, Lamp5 neurons enriched in superficial layers and Sst neurons in deeper layers. Regional preferences were also identified (Figure S6M). For instance, Sst and Reln neurons were enriched in the ILA area (Figure S6N), in line with the previous report.[35] Pvalb neurons had relatively lower densities in most regions associated with lateral and medial subnetworks, such as agranular insular posterior (AIp), but were more abundant in the RSP (Figures S6O–S6Q). Among Pvalb clusters, three (TE_N_GABA_PVALB_115/116/118) showed this pattern.

Although non-neuronal cells were more broadly distributed compared with neurons, some exhibited region-enriched patterns (Figures 1B, 2A, and S7A–S7C; Table S3). For example, among 7 astrocyte clusters, ASC_281 (*Agt*+) enriched in non-telencephalon areas, whereas ASC_283, identified as Bergmann glial[36] due to *Gdf10* expression, was specific to the cerebellum[3]

Figure 1. Construction of a cell-type atlas across mouse brains with high resolution

(A) Schematic of constructing the spatial transcriptome for mouse brains. Red circles mark cell boundaries in cell segmentation.

(B) Taxonomy tree showing 308 cell clusters identified based on snRNA-seq, each assigned a unique name and color. Bar plot indicates the fraction of cells according to region sources of snRNA-seq (OB, olfactory bulb; CTX, cerebral cortex; HIP, hippocampus; CNU, cerebral nuclei; TH, thalamus; HY, hypothalamus; MB, midbrain; P, pons; MY, medulla; CB, cerebellum. See abbreviations of regions in Table S10). Dot plot illustrates the expression of neurotransmitter-/neuromodulator-related genes for neurons in snRNA-seq (*Slc17a7* and *Slc17a6*, glutamatergic; *Gad1* and *Slc6a1*, GABAergic; *Hdc*, histaminergic; *Slc6a3*, dopaminergic; *Avp*, arginine vasopressin; *Gal*, galanin; *Hcrt*, hypocretin; *Tph2*, serotonergic; *Slc6a2*, noradrenergic; *Ucn*, urocortin; *Chat*, cholinergic).

(C) UMAP visualization of cell subclasses and clusters.

(D–F) Overview of cell-cluster distribution in representative coronal sections. (D) Sections were selected every 1 mm in mouse #1 (section no. and bregma coordinates shown, unit mm). (E and F) Zoomed-in views of regions labeled by red boxes in (D). Boundaries of cortical layer 4 (E) and locus coeruleus (F) are labeled by blue boxes and further magnified. Glutamatergic neurons colored in red and noradrenergic neurons in pink. Scale bars, 1 mm, 500 μm, and 50 μm. See also Figures S1–S5 and Tables S1, S2, and S10.

Please cite this article in press as: Han et al., Single-cell spatial transcriptomic atlas of the whole mouse brain, Neuron (2025), https://doi.org/10.1016/j.neuron.2025.02.015

CellPress

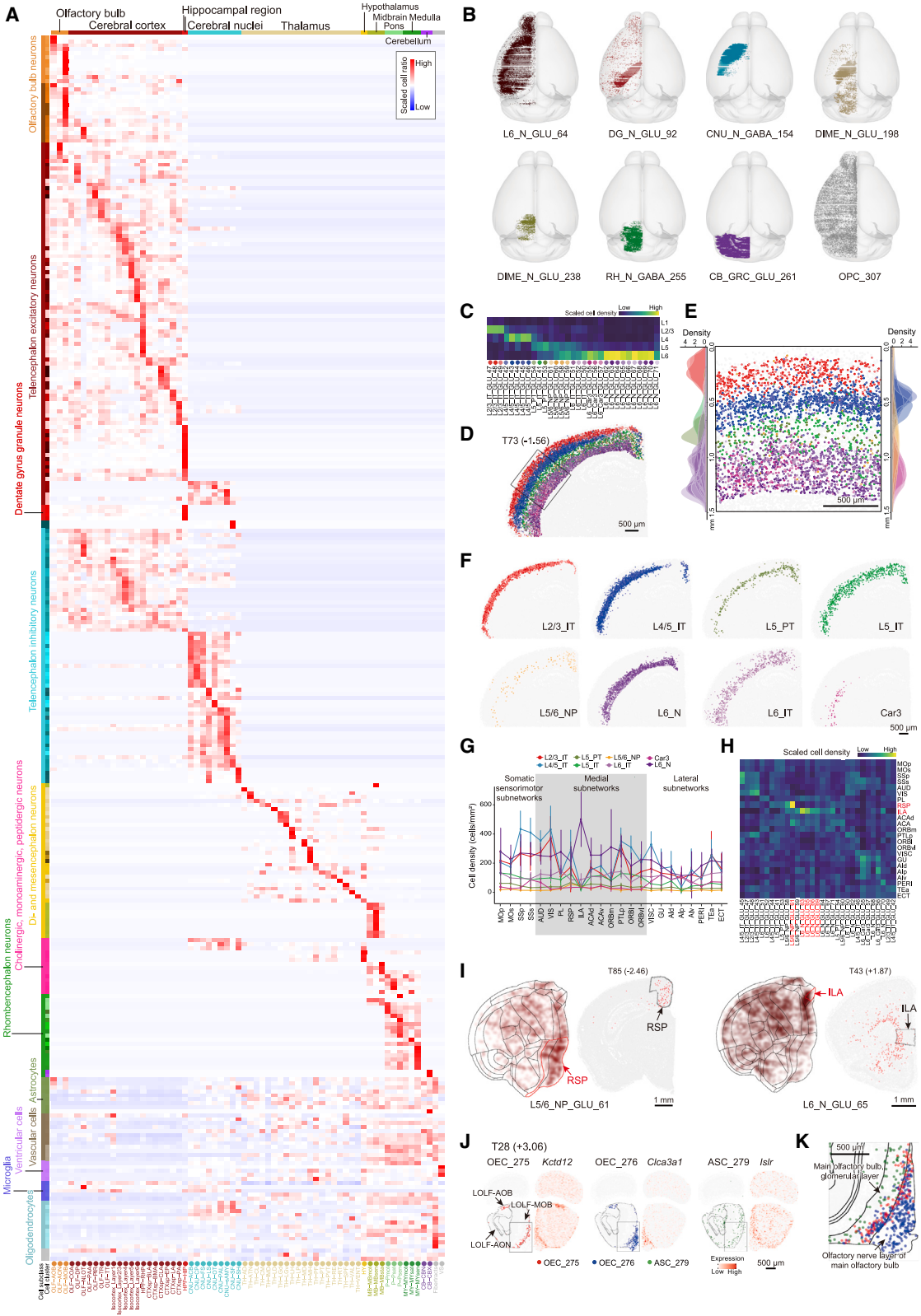

(legend on next page)

Please cite this article in press as: Han et al., Single-cell spatial transcriptomic atlas of the whole mouse brain, Neuron (2025), https://doi.org/10.1016/j.neuron.2025.02.015

(Figure S7D). In addition, we compared the spatial distribution of olfactory ensheathing cells (OECs) and astrocytes in the olfactory bulb subregions (Figures 2J and 2K). OECs, sharing partial molecular signatures with astrocytes (Figures S7E and S7F), localized in the outer layers of the olfactory bulb.[37,38] We demonstrated that two OEC clusters (OEC_275/276) were primarily localized in the accessory olfactory bulb (AOB) and main olfactory bulb (MOB). Meanwhile, an astrocyte cluster, ASC_279, was enriched in the MOB (Figure 2J). In the MOB and surrounding areas, ASC_279 was enriched in the glomerular layer, whereas OEC_276 was situated in the olfactory nerve layer. OEC_275, by contrast, was positioned at the boundary between these two layers (Figure 2K). Molecular profiles of these clusters exhibited differences, with *Kctd12* highly expressed in OEC_275, *Clca3a1* in OEC_276, and *Islr* in ASC_279 (Figure S7G). Further analysis revealed that ASC_279 exhibited stronger co-localization with two neuronal clusters (OB_N_GABA_174 and OB_N_GLU_177, Figure S7H and S7I), whereas OEC_275/276 did not, indicating closer interaction with OB neurons compared with OECs.

To investigate relationships between cell types and neurological diseases, we performed enrichment analysis across cell subclasses and clusters using marker genes and gene sets related to 123 brain diseases[30–32] (Figures S8A and S8B). In particular, we focused on Parkinson's disease, which is characterized by the progressive loss of dopaminergic neurons in the substantia nigra (SN), leading to dopamine reduction in the brain.[39,40] Our analysis revealed differences in proportions of two dopaminergic clusters (DIME_N_DOP_224/225) in the SN (Figure S8C). Moreover, these two clusters exhibited varying levels of enrichment within the Parkinson's disease-related gene set, with DIME_N_DOP_225 exhibiting higher expression of Parkinson's disease-related genes (Figure S8D). We found that DIME_N_DOP_225 was primarily localized in the SN, whereas DIME_N_DOP_224 was more diffusely distributed (Figures S8E and S8F). These distribution preferences may be linked to distinct brain functions and neurological diseases, providing a valuable resource for advancing our understanding of brain organization and guiding the development of targeted therapeutic strategies.

Distribution of the neuronal subtypes and region-enriched genes in the brainstem

The brainstem is vital for various physiological functions.[41,42] Combining snRNA-seq and Stereo-seq data, we identified 23 neuronal cell clusters and found regional preferences for several cell types (Figure 3A). For example, RH_N_GABA_257, RH_N_GLU_210, RH_N_GLU_240, and RH_N_GLU_252 were restricted in the nucleus of the trapezoid body (NTB), the parabrachial nucleus (PB), the principal sensory nucleus of the trigeminal (PSV), and the cochlear nucleus (CN), respectively (Figure S9A). Interestingly, NTB and CN were auditory nuclei, and the corresponding cell clusters, RH_N_GABA_257 and RH_N_GLU_252, were both positive for parvalbumin (Figure S9B). In contrast, non-neuronal cells did not show such regional distribution in the brainstem (Figure 2A).

Motor and neuromodulatory neurons were enriched in the brainstem. Consistently, cholinergic (RH_N_CHO_233), norepinephrinergic (RH_N_NOR_231), and serotonergic (RH_N_SER_229) neurons were enriched in the motor nuclei, the locus ceruleus (LC), and the raphe nuclei, respectively (Figures 3A and 3B; Video S2). Understanding whether diverse motor nuclei in the brainstem possess distinct molecular signatures has been challenging due to their small size, diffuse boundaries, and the lack of transcriptomic data uncontaminated by surrounding regions. Using Stereo-seq data, we revealed high-level heterogeneity in the motor nuclei of the trigeminal (V), facial motor nucleus (VII), hypoglossal nucleus (XII), and dorsal motor nucleus of the vagus nerve (DMX) (Figures 3C and S9C). For example, genes such as *Nrgn*, *Ttr*, *Gal*, and *Dag1* were enriched in specific motor nuclei (Figure 3D). Gene Ontology (GO) analysis also revealed functional differences across these nuclei (Figure S9D). Additionally, serotonergic neurons in different raphe nuclei also exhibited selective gene expression patterns (Figures 3E and 3F), highlighting gene expression diversity for cholinergic and serotonergic neurons with distinct spatial enrichment.

Region-enriched genes are critical for the physiological function of the brainstem. We further identified 155 genes (STAR Methods) highly expressed in 22 brainstem nuclei (Figures 3G and S9E). For example, *Pth2* and *Sst* were enriched in medial paralemniscal nucleus (MPL), as previously reported.[43] These genes mainly encode enzymes, receptor-related proteins, and neuropeptides (Figure S9F; Table S4). Notably, *Dbh*, which synthesizes norepinephrine, was highly expressed in the LC, whereas *Ddc* and *Tph2*, involved in serotonin synthesis, were enriched in the RAmb. Enzyme-related genes such as *Plpp4*, *Dpysl3*, and *Ache* were concentrated in the DMX. Several neuropeptides (*Nmb*, *Nps*, *Pth2*, *Rln3*, and *Ucn*) exhibited regional enrichment in the brainstem (Video S3). In addition, some genes exhibited subregional enrichment, such as *Barhl1* in the dorsal

Figure 2. Brain-wide distribution of cell clusters in the mouse brain

(A) Heatmap showing the distribution (*Z* score-scaled cell ratios) of 308 cell clusters across 66 brain areas.

(B) Spatial distribution of 8 representative cell clusters in the 3D mouse brain.

(C) Heatmap showing the scaled (*Z* score) densities of glutamatergic neurons across isocortical layers.

(D–F) Glutamatergic neuron distribution on coronal section T73, colored by cell clusters. Scale bar, 500 μm. (D) Merged view. (E) Zoomed-in view of the rectangle region in (D), with depth distribution. (F) Distribution of 8 glutamatergic groups.

(G) Density of 8 glutamatergic groups across cortical areas organized into 3 subnetworks.[33] Error bars were estimated across all cortical sections. Data are represented as mean ± SD.

(H) Heatmap of the scaled (*Z* score) densities of glutamatergic neurons across cortical areas.

(I) Distribution of L5/6_NP_GLU_61 and L6_N_GLU_65 on flatmap (left) and coronal sections (right) of T85 and T43. Scale bar, 1 mm.

(J and K) Distribution and marker gene expression of OECs and astrocytes (OEC_275, OEC_276, and ASC_279) individually. Scale bar, 500 μm. (J) Separated views. (K) Merged view of rectangle regions from (J).

See also Figures S6–S8, Table S3, and Video S1.

Please cite this article in press as: Han et al., Single-cell spatial transcriptomic atlas of the whole mouse brain, Neuron (2025), https://doi.org/10.1016/j.neuron.2025.02.015

CellPress

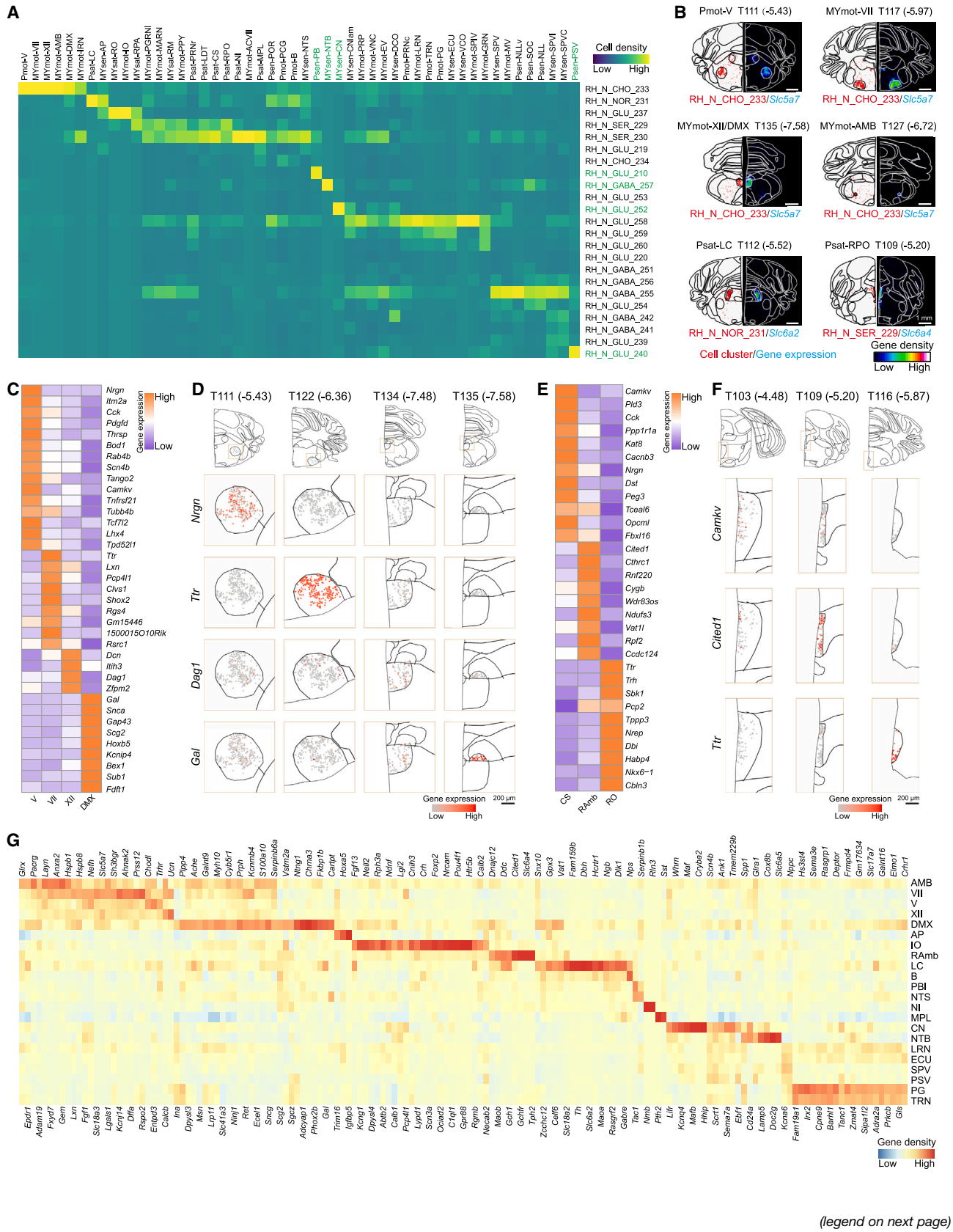

(legend on next page)

Please cite this article in press as: Han et al., Single-cell spatial transcriptomic atlas of the whole mouse brain, Neuron (2025), https://doi.org/10.1016/j.neuron.2025.02.015

CN and *Hhip* in the ventral CN (Figure S9G). Together, our analysis provided a map for the 23 neuronal cell clusters and revealed many region- or subregion-enriched genes in the brainstem.

Transcriptional-profile-based brain region parcellation and spatial distribution of gene modules

Traditional brain parcellation relied on cytoarchitecture and function, overlooking transcriptional properties. With the brain-wide spatial transcriptomic map, we examined whether brain region parcellation could be optimized. Specifically, we performed BayesSpace[44] clustering on the bin100 data (100 × 100 DNB spots, dimension size: 50 μm × 50 μm; STAR Methods) derived from 123 brain sections of mouse #1 brain (Figure 4A). We found many bin100 clusters exhibited brain-region-selective distribution (Figure S10A). Accordingly, gene-based brain region parcellation was performed based on region-selective clusters. We finally yielded 148 brain regions (Figure S11; STAR Methods), showing a consistency with ABA CCFv3 in 14 representative brain sections (Figures 4B and S10B). This was exemplified in section T74, showing that regions defined by transcriptomic data, like the cortex, hippocampus, thalamus, and caudate putamen (CP) in the striatum, exhibited high overlap with that of ABA CCFv3 (Figures 4C–4E).

Moreover, our gene-based brain region parcellation revealed that 8 brain regions could further be divided into finer subregions. For example, glomerular layer (MOBgl), granule layer (MOBgr) in MOB, and CP could be further separated into lateral and medial area, whereas the nucleus accumbens (ACB) and lateral hypothalamic area (LHA) possessed dorsal and ventral subregions. CA3 pyramidal layer (CA3sp) contained two subregions that are proximal or distal to dentate gyrus (DG). Besides, inferior colliculus (IC) had five layers arranged along its long axis; pontine central gray (PCG) can be divided into 2 segmentations (Figures 4F and S12A–S12H). We found that cortical subregions could be classified by spatial clustering of each single cortical layer; for example, we distinguished the primary cortical region from the associative region in layer 2/3. We also identified 6 subregions in the associative cortex (AId, AIv, AssoD, ORBl, ORBm, and ORBvl) and 2 sublayers in the primary cortex (L2 and L3) (Figure S12I). These were further confirmed by the data showing that subregions expressed distinct molecular markers. Marker genes for each brain region were detailed in Table S5. The reproducibility of parcellation was assessed between two mice. Co-clustering revealed consistent spatial patterns in bin100 clusters (Figure S10C), with highly correlated gene expression profiles across sections (Figure S10D). These results showed that brain region parcellation could be achieved based on spatial transcriptomic features.

To explore how co-expressed genes in different brain regions contribute to their functions, we calculated gene modules, groups of genes with similar spatial patterns, in 123 sections from mouse #1 using Hotspot, a spatially varying gene identification method,[45] based on the bin100 data. A total of 2,632 region-selective gene modules were identified (Table S5; STAR Methods). For example, there were 50 modules detected in the T74 section (Figure 4G), 34 of which exhibited regional selectivity (Table S5). The distribution of 12 modules was shown as examples (Figure 4H). Specifically, gene module 22 (G22), G18, G5, G10, G38, and G14 were enriched in different layers of the cortex. G26 was enriched in the piriform cortex (PIR). Notably, G9 and G11 were enriched in the ammon's horn (CA) and the DG regions of the hippocampus, respectively. G25, with *Pvalb* exhibiting the highest autocorrelation coefficient, was found in the reticular nucleus (RT) of thalamus, consistent with the known aggregation of mass Pvalb GABAergic neurons in RT.[46,47] The selective identity of gene modules for different brain regions or subregions was also confirmed by the distribution patterns of their representative genes (Figures 4I and S10E). GO analysis revealed that genes within these modules were relevant to the functions of their corresponding brain regions; for example, genes in G2 (fiber tracts) are associated with axon ensheathment and genes in G6 (hypothalamus) are associated with hormone secretion (Figure S10F). Additionally, gene module analysis also identified small nuclei not defined in CCFv3, like the MPL (Figure 4J). The stability of gene module analysis was verified by high correlation of spatial gene modules between two adjacent brain sections (Figures S10G–S10J).

Additionally, we examined gene module distribution in 3-dimensional space, focusing on the thalamus across 42 sections. Using Hotspot,[45] We found 9 gene modules in 3D within the thalamus (Figure 4K). G1 was restricted to the medial and lateral habenula nuclei (MH and LH), whereas others were found across multiple sub-areas (Figures 4L and 4M). Module scores and gene expression patterns indicated a subregional preference of each module, suggesting a different transcriptomic profile between the medial and lateral thalamus (Figure 4M).

Spatiotemporal profile of gene expression in the developing brain

The formation of brain regions is governed by sets of TFs and genes with distinct spatiotemporal profiles.[48–50] Our analysis above showed that some gene modules exhibited regional selectivity, so we asked whether this is also the case during development. Accordingly, we collected spatial whole-transcriptome data of developing mouse brain with 7 sagittal sections from embryonic to adult stage (clustered and annotated

Figure 3. Distribution of neuronal cell clusters and genes in the brainstem

(A) Heatmap showing the densities of different cell types in the brainstem nuclei.
(B) Spatial distribution of region-selective cell clusters (red) and marker genes (blue). Scale bar, 1 mm.
(C) Heatmap showing the expression of genes enriched in 4 motor nuclei.
(D) Expression of 4 representative genes in RH_N_CHO_233 cells in the 4 motor nuclei. Scale bar, 200 μm.
(E) Heatmap showing the selective expression of genes in 3 raphe nuclei.
(F) Expression of 3 representative genes in RH_N_SER_229 cells in the 3 raphe nuclei. Scale bar, 200 μm.
(G) Heatmap showing the 155 genes with regional preference in the brainstem nuclei.
See also Figures S9, Table S4, and Videos S2 and S3.

Please cite this article in press as: Han et al., Single-cell spatial transcriptomic atlas of the whole mouse brain, Neuron (2025), https://doi.org/10.1016/j.neuron.2025.02.015

CellPress

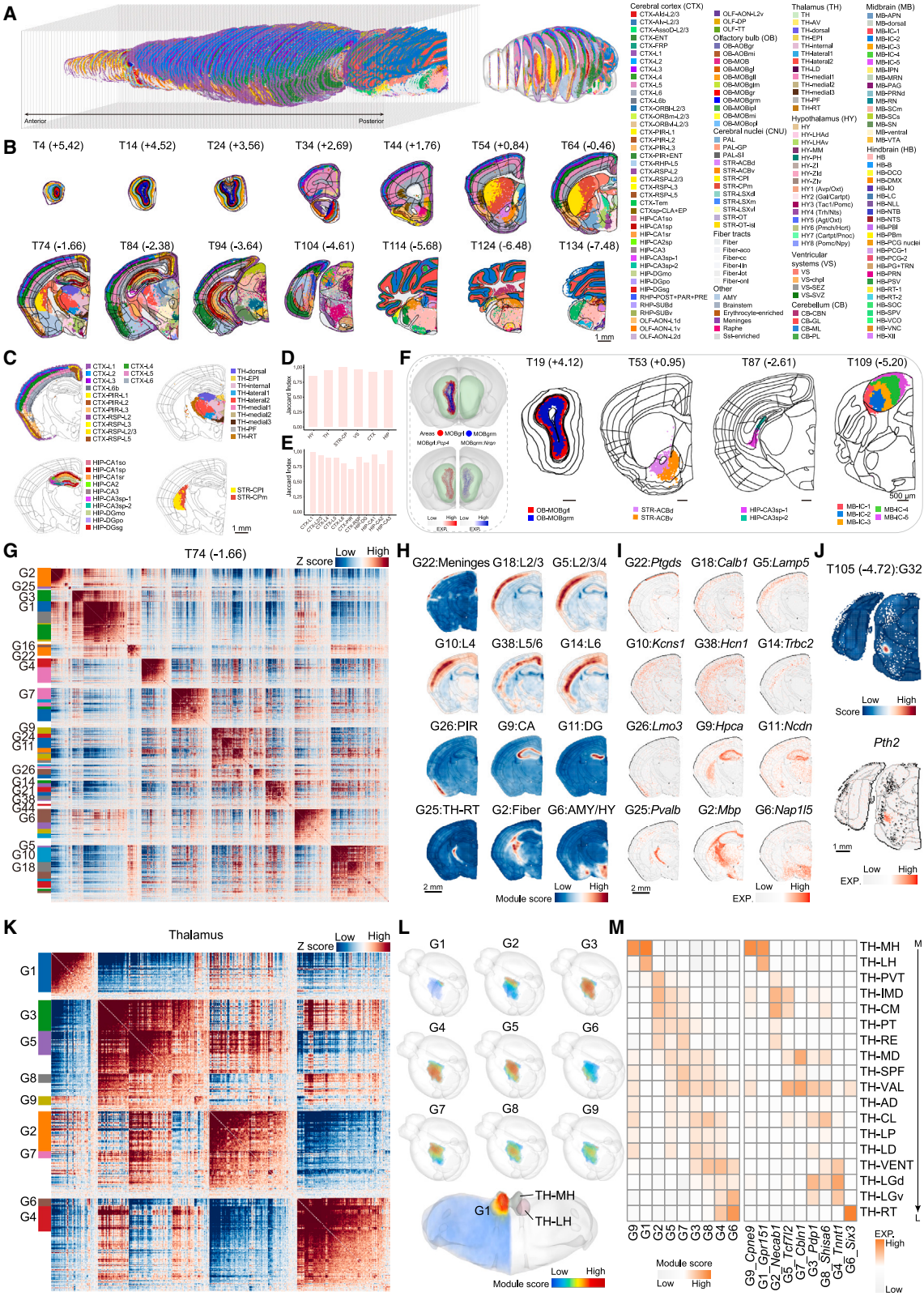

(legend on next page)

Please cite this article in press as: Han et al., Single-cell spatial transcriptomic atlas of the whole mouse brain, Neuron (2025), https://doi.org/10.1016/j.neuron.2025.02.015

similarly to coronal sections) (Figures 5A and S13A), including published data on embryonic day 12.5 (E12.5), E14.5, and E16.5[19] and post-natal day 7 (P7)[51] mice and newly generated data for P1, P14, and P77 mice.

Among the region-selective gene modules mentioned in the above section, we found 762 out of all 1,368 mouse TFs expressed in the 7 sagittal sections,[53] indicating distinct gene regulation networks (i.e., TF regulons) across different brain areas. Using SCENIC,[52] we identified 573 TF regulons with regional enrichment across 13 major brain regions of the adult stage (Figure S13B) and a total of 998 TF regulons for the 7 developmental stages. Furthermore, we applied Hotspot[45] on each section, resulting in a total of 150 clusters, each of which contains a group of spatially co-localized TF regulons (Figure 5B; Table S6). GO enrichment analysis found that regulons within each cluster were related to distinct biological processes (Figure 5B), and 144 out of 150 clusters were found localized in major brain regions (Figure 5C), suggesting that these spatial co-localized regulons could work together during brain region development.

Next, we asked how the activities, as defined by an expression-based metric from SCENIC,[52] of these region-selective TF regulons change during development. In the cortex, 68 TF regulons exhibited higher activity during embryonic stages, whereas 76 exhibited higher activity in post-natal stages (Figure 5D). In the striatum, we found that 52 TF regulons were more abundant in early periods whereas 56 were abundant in later periods (Figure 5D). We also found a similar pattern for 77 and 65 TF regulons in the thalamus and cerebellum, respectively (Figure 5D). For example, TFAP2C (names all in capital letters stand for TF regulons) was found to be abundant in the embryonic cortex and developing olfactory area (Figure 5E), where the core gene *Tfap2c* was considered a key TF determining cortex radial glia fate in a recent study.[54] In the striatum, PAX9 was enriched in embryonic age, whereas FOXO1 was gradually enriched during post-natal development (Figure 5E), consistent with previous reports in the developing mouse striatum.[55] As for individual genes, 33 genes were found to maintain a region-selectivity in the cortex, striatum, or thalamus across all 7 stages, whereas 385 genes showed brain-regional selectivity only at a certain stage (Figure S13C). The comprehensive dynamics of region-selective regulons and genes was summarized in Table S6.

The cortex was organized as both laminar and columnar structures during development, which is determined by transcriptional programs.[56] We examined transcriptional regulation across the dorsal-ventral axis or rostral-caudal axis during development using Spateo.[57] In analysis of the dorsal-ventral axis, we found 206 regulons showing laminar-related distribution (Table S6). For example, ATF4 gradually shifted from the superficial layer to the middle layer (Figure 5F). TBR1 shifted from the superficial layer to the deep layer, in line with the prior maturation of layer-6 cortical neurons.[58,59] NR2E1 shifted from the deep layer to the superficial layer (Figure 5F), which aligns well with the important function of *Nr2e1* in neural stem cell proliferation[60,61] and its crucial role for the intactness of the supragranular layer.[62] As for the rostral-caudal axis, we found 22 TFs exhibiting spatial increment or decrement gradient (Figure S13D; Table S6). *Lhx2* showed a similar increment along the rostral-caudal axis as *Nfix* in embryonic stages (E12.5, E14.5, and E16.5), but the pattern was weakened in post-natal stages (P1, P7, P14, and P77) (Figure 5G). This seems in line with previous reports showing the gradient distribution of *Lhx2* at E15.5 stage and its crucial role in barrel column formation,[63,64] a process mostly in embryonic stages.[65] We also found 134 non-TF genes exhibiting rostral-caudal gradients (Figures 5G and S13D; Table S6). These gradient distributions of TFs and genes could be involved in defining the cortical organization patterns.

Next, we examined the kinetics of several neural developmental events using a gene set enrichment scoring method (STAR Methods). Our analysis showed that three major neurodevelopmental event-associated gene sets exhibited the dynamic change across 9 brain regions and 7 stages (Figures S13E–S13G). Specifically, genes involved in gliogenesis and synapse maturation showed higher enrichment in post-natal stages, whereas genes associated with neuroblast proliferation were enriched in embryonic stages. The genes involved in gliogenesis started to show enrichment around birth and quickly reached peak level at P14. Interestingly, we found higher levels of gliogenesis-related gene enrichment in the fiber tracts and hindbrain as compared with others, consistent with the recent report in human brain gliogenesis.[66] In addition, genes involved in synapse maturation were gradually enriched at the very beginning of embryonic stages and reached steady state after birth (Figure S13G).

Figure 4. Spatial gene profiles of adult mouse brain

(A–C) Brain region parcellation using Stereo-seq bin100 clustering. (A) Overview of 123 annotated sections from mouse #1 brain (left) and 3D illustration of 14 representative sections (right). (B) Visualization of 14 representative sections (section no. and bregma coordinates shown, unit mm). Scale bar, 1 mm. (C) Separated views of regions in T74 section.

(D and E) Quantification of Jaccard similarity between molecularly defined brain regions and ABA CCFv3. (D) For large regions (CTX, TH, HIP, and CP). (E) For subregions within CTX and HIP.

(F) Subregions of 4 representative brain regions (MOBgr, ACB, CA3sp, and IC). The dotted box shows a 3D illustration (upper) and feature gene expression (lower) of lateral and medial subregion of MOBgr. Black lines indicate CCFv3 boundaries. Scale bar, 500 μm.

(G) Heatmap showing the genes with significant spatial autocorrelation grouped into different gene modules in T74 section, with 20 spatially selective gene modules highlighted.

(H and I) Gene modules with regional preference. Scale bar, 2 mm. (H) Module score distribution. (I) Expression of representative genes in modules.

(J) Gene module score distribution in the MPL and expression of the representative *Pth2* gene. Scale bar, 1 mm.

(K) Heatmap showing the genes with significant spatial autocorrelation grouped into different gene modules in the whole thalamus.

(L) Visualization of 9 gene modules associated with thalamic subregions in 3D (upper). Module G1 highlighted (bottom).

(M) Gene module selectivity in the 3D thalamus is presented with enrichment scores in subregions (left) and a heatmap of representative gene expressions (right), with thalamic subregions ordered along the medial-lateral axis, indicated by the vertical arrow.

See also Figures S10–S12, Tables S5 and S11, and Videos S2 and S3.

Please cite this article in press as: Han et al., Single-cell spatial transcriptomic atlas of the whole mouse brain, Neuron (2025), https://doi.org/10.1016/j.neuron.2025.02.015

CellPress

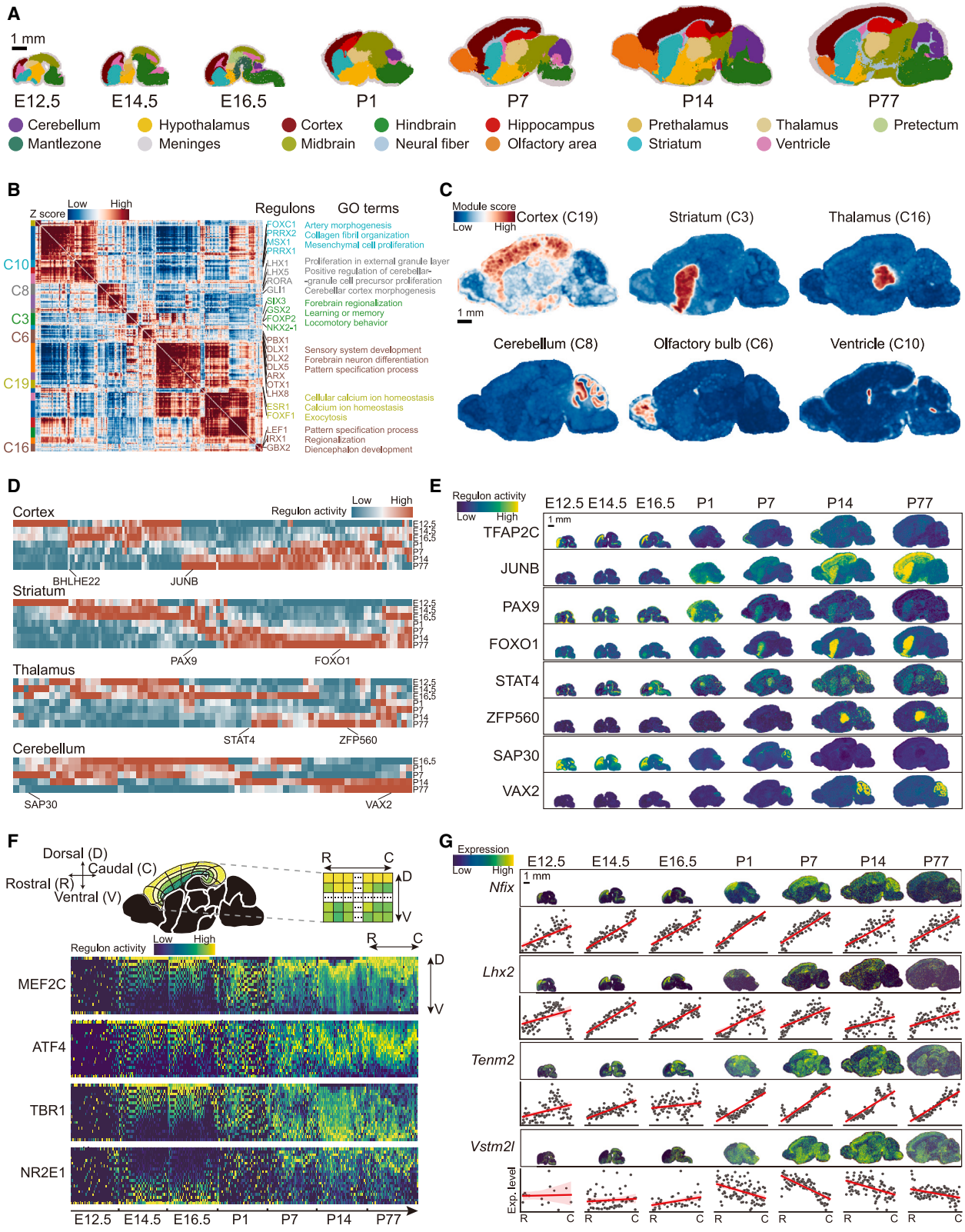

(legend on next page)

Spatiotemporal profile of lncRNA in the brain

In the mammalian genome, less than 3% of the genome is transcribed into protein-coding transcripts, whereas the majority are ncRNAs, with some exceeding 200 bp, termed as lncRNAs).[67] Although previous studies have characterized some lncRNAs in the mouse brain,[67,68] a comprehensive analysis of their spatial distribution was lacking. Among 9,580 known mouse lncRNAs, we detected 5,834 lncRNAs in our adult mouse brain Stereo-seq dataset, with 513 lncRNAs showing regional enrichment (Figure 6A; Table S7; STAR Methods). For examples, *Gm12688*, *Gm33651*, *6330420H09Rik*, *Gm20649*, *Hotairm1*, and *Gm14033* exhibited preferential expression in olfactory areas, striatum, hippocampus, hypothalamus, medulla, and cerebellum, respectively (Figures 6B and 6C; Video S4). Moreover, 37 lncRNAs showed layer-enriched distribution in the cortex (Figure 6D), with *Gm26870*, *A830009L08Rik*, *1700047F07Rik*, *Gm11730*, and *Gm28928* enriched in L1, L2/3, L4, L5, and L6, respectively (Figure 6E).

Some lncRNAs are known to be crucial for brain development.[69–71] To identify those potentially involved in neurodevelopment, we performed Hotspot analysis on Stereo-seq data from E12.5 to P77, revealing 184 gene modules, 160 of which showed brain region preference (Table S8), with P14 data presented as an example (Figures S14A and S14B). We then identified 216 lncRNAs with spatiotemporal dynamics (60 for cortex, 73 for striatum, 30 for thalamus, and 95 for cerebellum) across development stages (Figures S14C and S14D). For example, *A930024E05Rik* was highly abundant in the embryonic cortex,[72] whereas *AC129186.1* peaked in the post-natal period (Figures 6F and 6G). Several region-enriched lncRNAs, such as *Gm11266* (cortex),[73] *D430036J16Rik* (striatum),[2] *Gm2694* (cerebellum),[74,75] *Gm15577* (cerebellum),[76] were also reported in previous studies. However, most lncRNA expression patterns remain unknown. Interestingly, some cerebellum-enriched lncRNAs, such as *Gm2694* and *Lhx1os*, show expression patterns that coincide with cerebellar development starting from E16.5 (Figure S14D). *Gm2694* has been shown to regulate synaptic stability in the cerebellum, indicating its potential role in cerebellar development.[74,75] These findings suggest that lncRNAs exhibiting spatiotemporal expression patterns may play important roles in brain morphogenesis during development.

Genes within the same modules are often functionally related.[77] To predict the potential roles of lncRNAs in development, we performed GO functional enrichment analysis on brain-region-selective gene modules. Early-stage modules (E12.5–E16.5) were primarily associated with neuronal development (Figures 6H, 6I, S14E, and S14F), suggesting that lncRNAs in these modules may be involved in brain development. At later stages (P1–P77), modules became enriched with genes related to brain-region-specific functions. For example, in the striatum, post-natal modules (including 36 lncRNAs) were linked to the dopamine receptor signaling pathway (Figures 6H and 6I), whereas in the cortex, modules (including 15 lncRNAs) were associated with synapse maturation (Figure S14E). In the cerebellum, post-natal modules (including 46 lncRNAs) were linked to the GO term of parallel fiber to Purkinje cell synapse (Figure S14F). These findings suggest that lncRNAs may regulate brain-region-specific functions during later stages. Overall, lncRNAs with spatiotemporal expression patterns likely contribute to both early embryonic neural development and later neural function, though further experimental studies are needed to confirm their roles.

Recent studies indicate that lncRNA transcription is linked to nearby gene transcription, sharing promoter regions.[78–80] Divergent lncRNAs transcribe from the same promoter as adjacent mRNAs but on opposite strands, whereas convergent lncRNAs transcribe toward adjacent mRNAs on opposite strands, often overlapping.[81] Although expression patterns of these lncRNA-mRNA pairs have been studied in cells and tissues,[78,82] their spatial brain expression remains largely unknown. To investigate this, we categorized lncRNA-mRNA pairs into divergent (2,503 pairs) and convergent (4,480 pairs) groups based on the genomic distance between their transcription start sites (STAR Methods). In our spatial transcriptomic analysis of the adult mouse brain, we identified 3,049 lncRNA-mRNA gene pairs, with 1,019 divergent and 2,030 convergent pairs (Table S9). We discovered that divergent pairs had a significantly higher expression correlation than convergent pairs across different brain regions (Figure 6J). Notably, 18 convergent pairs exhibited antagonistic expression patterns, such as the *Airn-Mas1* pair, which showed negative correlation in various regions (Figures 6K and 6L). Similarly, the *Gm45441-Grin2d* pair displayed opposing expression levels (Figures S14G and S14H). Further analysis revealed that 103 convergent gene pairs had distinct antagonistic expression in different cell types. For instance, *Gm13944* was more highly expressed than *Zfp385b* in Purkinje cells but less in granule cells (Figures 6M and S14I). Stereo-seq data confirmed these spatial distribution differences, with *Gm13944* highly expressed in the Purkinje cell layer and

Figure 5. Spatial transcriptional profile of developmental mouse brain

(A) Clusters generated by unsupervised spatial constrained clustering (SCC) of sections across E12.5–P77. Scale bar, 1 mm.

(B) Heatmap showing TF regulons with high spatial autocorrelation grouped into clusters (e.g., C3 and C6), and correlated to distinct GO biological processes.

(C) Spatial distribution of 6 region-selective TF regulon clusters in P14 sagittal brain section as examples. Scale bar, 1 mm.

(D) Heatmap illustrating the TF regulon activities in the developing cortex, striatum, thalamus, and cerebellum. Regulon activity was calculated using AUCell-SCENIC.[52]

(E) Visualization of regulon activities of 8 TF regulons in the developing cortex, striatum, thalamus, and cerebellum. Scale bar, 1 mm.

(F) Top: sketch of the orthogonal visualization for cortical laminar-columnar structure. Bottom: heatmap showing the spatial enrichment of 4 example TF regulons along the dorsal-ventral axis in the developmental cortex.

(G) Visualization of dynamic changes of genes with rostral-caudal gradient in developing cortices. The gradient distribution of each gene at each stage is demonstrated using an auxiliary scatterplot, with black dots indicating the mean expression on each relative rostral-caudal position, and a red line showing the linear regression of these points. Scale bar, 1 mm.

See also Figures S13 and Table S6.

Please cite this article in press as: Han et al., Single-cell spatial transcriptomic atlas of the whole mouse brain, Neuron (2025), https://doi.org/10.1016/j.neuron.2025.02.015

CellPress

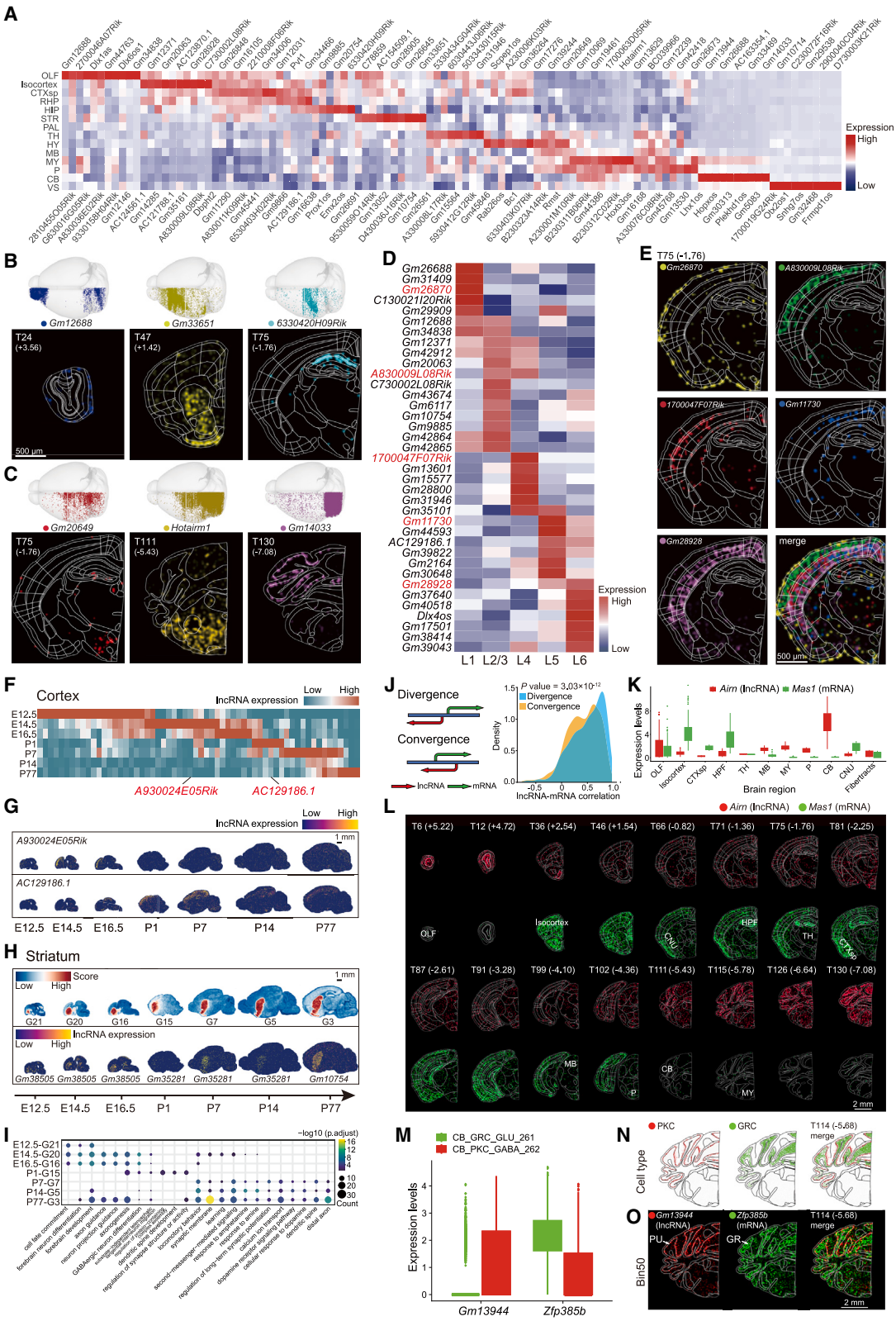

(legend on next page)

Please cite this article in press as: Han et al., Single-cell spatial transcriptomic atlas of the whole mouse brain, Neuron (2025), https://doi.org/10.1016/j.neuron.2025.02.015

Zfp385b in the granule cell layer of the cerebellum (Figures 6N and 6O). Among these 103 gene pairs, 18 gene pairs also exhibited antagonistic expression trends in different brain regions, as mentioned above (Figure S14J). Our findings provide valuable insights into the spatial expression patterns of lncRNA-mRNA pairs in the mouse brain, highlighting their potential regulatory functions.

DISCUSSION

The mammalian brain possesses a remarkably intricate organization. In this study, we constructed a single-cell-resolution spatial transcriptomic atlas of the mouse brain with genome-wide coverage of most genes in the genome, including lncRNAs. By leveraging the spatial profile of the whole transcriptome, we precisely delineated brain regions with the spatial clustering method across the whole brain, including several novel subregions. Our atlas provided a spatiotemporal map of gene expression from embryonic to adult stages, revealing numerous TF regulons and lncRNAs with distinct spatiotemporal dynamics. These findings lay a foundation for understanding the complex interactions among diverse cell types and the neural mechanism underlying animal behavior.

Brain-wide distribution of diverse cell types

Our study extends the understanding of the spatial organization of diverse cell types in the mouse brain, revealing their distinct laminar and regional distribution patterns that align with brain function and disease relevance. For instance, glutamatergic neurons exhibited laminar distribution in the cortex, while certain clusters were enriched in specific cortical regions. In the ILA, the area related in mood and affective disorder,[83] we identified neuron clusters enriched with depression-related expression profiles, suggesting a potential role in mood regulation. A recent study of the macaque cortex highlighted variations in cellular configurations correlated with the hierarchical structure of the visual system.[84] This supports the idea that the enrichment of cell types in cortical regions plays a critical role in both brain function and diseases.

In the brainstem, we observed nucleus-enriched clusters, such as glycinergic interneurons in the NTB as documented[85] and glutamatergic neurons in CN. Notably, both clusters were *Pvalb*-positive. Pvalb interneurons are widely distributed in the auditory system, are well-tuned for sound frequency,[86] and enhance temporal coding in the auditory pathway.[87] The distinct distribution of glutamatergic and GABAergic Pvalb neurons across auditory nuclei suggests their specialized roles in auditory information processing. Together, these findings underscore the importance of our transcriptomic atlas for annotating cell types and elucidating their roles in brain function and pathology.

Brain-region-enriched modules and gene expression

Although mRNA distribution in the brain has been examined by ISH,[2,88] these data were collected in different animals, which often confounds analysis of gene expression patterns across the whole brain. With the 123 coronal brain sections from a single mouse brain, our atlas provided the opportunity for integrated analysis, especially in a 3D manner. We comprehensively identified brain region-selective genes, especially within brain regions such as the thalamus and brainstem nucleus.

Besides, whole-transcriptome coverage has enabled us to profile a large number of less-studied lncRNAs. Our findings extended the existing knowledge regarding brain-regional or subregional enrichment of numerous lncRNAs, suggesting that these lncRNAs may be crucial for the formation of brain regions. For instance, the antagonistic expression of convergent gene pairs such as *Airn* and *Mas1* suggests potential functional interference. Furthermore, we identified lncRNAs with spatiotemporal dynamics during brain development. Some of them have been studied previously. For example, *A930024E05Rik*, highly expressed in the developing cortex, is essential for cortical projection neuron differentiation and migration,[72] whereas *Gm2694*, associated with cerebellar development, influences synapse density and motor function.[74,75] The identification of lncRNAs with distinct spatiotemporal dynamics paved the way for further analysis of their functional roles.

Moreover, spatial transcriptomic data enabled the identification of molecular differences in neurons across small nuclei, such as cholinergic neurons in distinct motor nuclei of the brainstem, which is difficult to achieve with single-cell sequencing. For instance, hypoglossal nuclei genes were linked to diverse

Figure 6. Spatial profile of lncRNA in mouse brain

(A) Heatmap of region-enriched lncRNAs in 14 brain regions.
(B and C) Whole-brain distribution (upper) and spatial expression (lower) of 6 lncRNAs in brain sections (section no. and bregma coordinates shown, unit mm). Scale bar, 500 μm.
(D) Expression heatmap of 37 cortical-layer-enriched lncRNAs. Examples in (E) marked in red.
(E) Spatial distribution of 5 lncRNAs in coronal section T75. Scale bar, 500 μm.
(F) Dynamic expression changes of lncRNAs in developing cortex.
(G) Spatiotemporal distribution of cortical-enriched lncRNAs across development stages. Scale bar, 1 mm.
(H) Distribution of striatum-selective modules and their lncRNA expression across development stages. Scale bar, 1 mm.
(I) GO enrichment pathways of striatum-selective modules across development stages.
(J) Pearson correlation distribution (right) of convergent and divergent gene pairs (cartoon shown on left).
(K) Expression levels of *Airn-Mas1* convergent gene pair in different brain regions.
(L) Spatial distribution of *Airn-Mas1* pair in 16 sections. Scale bar, 2 mm.
(M) Expression of *Gm13944-Zfp385b* pair in cerebellar cell clusters of granule cells (CB_GRC_GLU_261) and Purkinje cell (CB_PKC_GABA_262).
(N) Distribution of *Gm13944-Zfp385b* convergent gene pairs in cell types of Purkinje (red) and granule (green) cells in section T114.
(O) Expression of *Gm13944* (red) and *Zfp385b* (green) in Purkinje (PU) and granule cell layer (GR), respectively. Scale bar, 2 mm.
See also Figures S14, Tables S7, S8, and S9, and Video S4.

physiological processes, including heart contraction and immune response, aligning with studies implicating this region in perinatal lung inflammation[89] and sudden unexplained perinatal death.[90] The identification of region-selective genes would facilitate our understanding of the function of these small nuclei.

Parcellation of brain areas based on transcriptomic profile

Traditionally, the boundaries of brain regions have been defined based on cytoarchitecture and function.[1,91,92] Our analysis defined the boundaries of 148 mouse brain areas based on spatial transcriptomic properties, largely consistent with ABA CCFv3.[27] This supports the transcriptomic basis of brain parcellation, consistent with a recent study.[12] Given that our transcriptomic data have high spatial resolution, our analysis allowed for a more detailed division of certain brain regions, such as the CP further divided into CPl and CPm, and ACB into ACBd and ACBv, identifying subdivisions not present in the ABA CCFv3. However, the functional relevance of these finer parcellations remains to be determined. Transcriptome-based parcellation is likely to enable studies of other less-studied species, where common parcellation frameworks of brains or other organs are not available.

Spatiotemporal analysis of transcriptome for the developing mouse brain

Our atlas also included a comprehensive spatiotemporal map of gene expression from embryonic to adult stage, exceeding existing works that only covered limited genes or stages. This has enabled the identification of 411 TFs with drastic spatiotemporal dynamics. For example, TFAP2C is enriched in the cortex during early development and involved in regulating cell fate of cortical radial glia.[54] These TFs regulons likely play roles in brain development, providing a valuable resource for neurodevelopmental research.

Further analysis showed that some of the TF regulons exhibited delicate spatiotemporal patterns within specific brain regions. In the developing cortex, we showed that 206 TF regulons exhibited laminar enrichment along the dorsal-ventral axis, and 156 genes showed gradient distribution on the rostral-caudal axis. For example, *Lhx2* displayed a rostral-caudal gradient, consistent with a previous study.[93] This gradient distribution pattern was thought to be important for the formation of sub-structures.[56] Consistently, it has been shown that *Lhx2* is involved in barrel cortex formation.[63] These TF regulons or genes showing gradient distribution are likely crucial in shaping cortical structure. Our study significantly extended previous findings[56] and revealed hundreds of genes exhibiting rostral-caudal axis gradient patterns across developmental stages, with their functional roles yet to be experimentally explored.

In summary, our study has constructed a 3D single-cell-resolution spatial transcriptome atlas for the mouse brain, mapping the spatial distribution of genes and cell clusters. This revealed region-selective cell clusters and genes, including lncRNAs, and demonstrated precise brain area definitions based on transcriptomic analysis. Moreover, we identified numerous TF regulons with spatial and temporal selectivity. The construction of a mouse brain atlas with single-cell resolution provides the basis for further exploring the mechanisms underlying physiological processes and development of the mouse brain.

Limitations

There are several limitations in this study. First, the limited capture efficiency of gene transcripts in spatial transcriptomics could result in lower detection of low-expressed genes, a common issue for *in situ*-based spatial transcriptomics methods.[4] Consequently, we could have missed some genes with low-expression levels in our spatial transcriptomic analysis. In fact, we identified 668 genes for one cell on average, which was insufficient for precise cell annotation. Therefore, we adopted Spatial-ID, an integrating transfer learning and spatial embedding strategy,[29] to perform precise cell-type annotation for spatial transcriptomic datasets based on our snRNA-seq data. Second, sparse brain sectioning and sampling points limited the resolution and depth of developing brain analysis. Third, coronal sections at 100-μm intervals in Stereo-seq may have missed small nuclei and disrupted brain region continuity. Therefore, the sampling of the brain with smaller spatial intervals, or even profiling all sections across the whole brain, would be needed for a more precise 3D whole-brain single-cell transcriptomic atlas in the future.

RESOURCE AVAILABILITY

Lead contact

Further information and requests for the resources and reagents may be directed to and will be fulfilled by the lead contact, Yan-Gang Sun (yangang.sun@ion.ac.cn).

Materials availability

All materials used for Stereo-seq and snRNA-seq are commercially available.

Data and code availability

The processed data are ready for exploration and may be accessed online (https://doi.org/10.12412/BSDC.1699433096.20001). All raw data produced in this study have been deposited to the CNGB Nucleotide Sequence Archive (accession code CNGB: CNP0003837). Additional information required to reanalyze the data reported in this paper is available from the lead contact upon request.

ACKNOWLEDGMENTS

This paper is from the Mesoscopic Brain Mapping Consortium. We thank H.B. Chen from Tencent AI lab for helping in data analysis. This work was supported by the National Science and Technology Innovation 2030 Major Program (2021ZD0204400), Shanghai Municipal Science and Technology Major Project (grant no. 2018SHZDZX05), the National Natural Science Foundation of China (nos. 32221003 and 32430038), the Scientific Instrument Developing Project of CAS (no. YJKYYQ20190052), National Key R&D Program of China (nos. 2022YFC3400400, 2022YEF0203200, and 2022YFA1603604), the Youth Innovation Promotion Association of the Chinese Academy of Sciences (no. 2022268, to C. Li), Guangdong Provincial Key Laboratory of Genome Read and Write (2017B030301011), and New Cornerstone Science Foundation through the XPLORER PRIZE. We sincerely thank the technical support provided by China National GeneBank and STOmics DCS Cloud.

AUTHOR CONTRIBUTIONS

H. Wang, J.D., Y. Zhong, J. Lin, Yu Chen, M.X, B.R., M. Cheng, Q.Y., X. Song, Y. Lu, N.Y., S.S., Y.A., W.D., X. Sun, S.Z., Y.D., Y.Z., J.X., S.W., W.T., Y. Liu, M. Chen, C. Xie, B.B., X.Z., Z.C., J.F., S. Li, Y.J., X.T., G.Z., H. Li, Y. Liu, Jianfeng Liu, M.H., J. Wang, Jiabing Liu, H.Z., Y.S., S.Y., X.J., G.W., C.W., X. Liu,

Xiangjie Xu, H. Cao, H. Zheng, Yadong Chen, H. Lu, Z.Y., J.Z., B.W., Z.W., Q.X., S.P., C. Liu, and C. Xu performed Stereo-seq and snRNA-seq experiments. Lei Han, Zhen Liu, Z.J., Y. Liu, Y. Peng, H. Chang, J. Lei, K.W., Y. Xu, W.L., Z. Wu, Q.L., X. Shi, M.Z., H.P., R.Z., J. Wu, Y.T., Y.W., Luyao Han, Q.Z., D.W., Y.B., Y. Liang, M.L., Y.X., Q.T., Y. Liu, H. Wen, Y.Y., X. Liao, H. Liu, N.F., K.M., and T.H. analyzed the data. L.C., Y. Li, S. Liu, S. Liao, A.C., Q.-F.W., J. Wang, Zhiyong Liu, J.M., and H.Y. provided important advice for the project and comments on the manuscript. X.W., C. Li, J.Y., Xun Xu, L.L., Z.S., W.W., and Y.-G.S. designed and supervised the study.

DECLARATION OF INTERESTS

Employees of BGI have stock holdings in BGI.

DECLARATION OF GENERATIVE AI AND AI-ASSISTED TECHNOLOGIES IN THE WRITING PROCESS

During the preparation of this work, the authors used ChatGPT 4.0 in order to improve the grammar of the manuscript. After using this tool, the authors reviewed and edited the content as needed and take full responsibility for the content of the publication.

STAR★METHODS

Detailed methods are provided in the online version of this paper and include the following:

- KEY RESOURCES TABLE
- EXPERIMENTAL MODEL AND STUDY PARTICIPANT DETAILS
  - Animals
- METHOD DETAILS
  - Brain tissue collection for Stereo-seq
  - Tissue cryosection, section flattening and RNA quality control
  - Stereo-seq experiment procedure
  - Stereo-seq library construction and sequencing
  - Processing of Stereo-seq raw data
  - Quality control of Stereo-seq sections
  - Cell segmentation
  - Gene-based brain region parcellation
  - Image registration and anatomy-based parcellation
  - 3D reconstruction of coronal sections
  - Sample preparation for single-nucleus sequencing
  - Single-nucleus suspension preparation
  - Single-nucleus library preparation and sequencing
  - Single-nucleus raw data processing
  - Single-nucleus data filtering
  - Single-nucleus iterative clustering and classification
  - Single-nucleus cluster dendrogram construction
  - Independence test of nuclei clusters
  - Single-nucleus data co-clustering with published dataset
  - Stereo-seq cell type transfer
  - Evaluation of cell type transfer consistency and accuracy
  - Analysis of cell type distribution across brain regions
  - Regulon analysis
  - Identification of spatial gene modules
  - Gene ontology analysis and enrichment scoring
  - Spatial expression pattern analysis
  - Identification of region-enriched genes
  - Identification of convergent and divergent gene pairs
  - Calculation of lncRNA-mRNA gene pairs
- QUANTIFICATION AND STATISTICAL ANALYSIS
- ADDITIONAL RESOURCES

SUPPLEMENTAL INFORMATION

Supplemental information can be found online at https://doi.org/10.1016/j.neuron.2025.02.015.

Received: April 22, 2024
Revised: October 24, 2024
Accepted: February 14, 2025
Published: July 9, 2025

REFERENCES

1. Franklin, K.B.J., and Paxinos, G. (2019). Paxinos and Franklin's the Mouse Brain in Stereotaxic Coordinates, Compact: The Coronal Plates and Diagrams (Academic Press).
2. Lein, E.S., Hawrylycz, M.J., Ao, N., Ayres, M., Bensinger, A., Bernard, A., Boe, A.F., Boguski, M.S., Brockway, K.S., Byrnes, E.J., et al. (2007). Genome-wide atlas of gene expression in the adult mouse brain. Nature *445*, 168–176. https://doi.org/10.1038/nature05453.
3. Zeisel, A., Hochgerner, H., Lönnerberg, P., Johnsson, A., Memic, F., van der Zwan, J., Häring, M., Braun, E., Borm, L.E., La Manno, G., et al. (2018). Molecular Architecture of the Mouse Nervous System. Cell *174*, 999–1014.e22. https://doi.org/10.1016/j.cell.2018.06.021.
4. Cheng, M., Jiang, Y., Xu, J., Mentis, A.A., Wang, S., Zheng, H., Sahu, S.K., Liu, L., and Xu, X. (2023). Spatially resolved transcriptomics: A comprehensive review of their technological advances, applications, and challenges. J. Genet. Genomics *50*, 625–640. https://doi.org/10.1016/j.jgg.2023.03.011.
5. Zhang, M., Eichhorn, S.W., Zingg, B., Yao, Z., Cotter, K., Zeng, H., Dong, H., and Zhuang, X. (2021). Spatially resolved cell atlas of the mouse primary motor cortex by MERFISH. Nature *598*, 137–143. https://doi.org/10.1038/s41586-021-03705-x.
6. Wang, X., Allen, W.E., Wright, M.A., Sylwestrak, E.L., Samusik, N., Vesuna, S., Evans, K., Liu, C., Ramakrishnan, C., Liu, J., et al. (2018). Three-dimensional intact-tissue sequencing of single-cell transcriptional states. Science *361*, eaat5691. https://doi.org/10.1126/science.aat5691.
7. Ståhl, P.L., Salmén, F., Vickovic, S., Lundmark, A., Navarro, J.F., Magnusson, J., Giacomello, S., Asp, M., Westholm, J.O., Huss, M., et al. (2016). Visualization and analysis of gene expression in tissue sections by spatial transcriptomics. Science *353*, 78–82. https://doi.org/10.1126/science.aaf2403.
8. Rodriques, S.G., Stickels, R.R., Goeva, A., Martin, C.A., Murray, E., Vanderburg, C.R., Welch, J., Chen, L.M., Chen, F., and Macosko, E.Z. (2019). Slide-seq: A scalable technology for measuring genome-wide expression at high spatial resolution. Science *363*, 1463–1467. https://doi.org/10.1126/science.aaw1219.
9. Stickels, R.R., Murray, E., Kumar, P., Li, J., Marshall, J.L., Di Bella, D.J., Arlotta, P., Macosko, E.Z., and Chen, F. (2021). Highly sensitive spatial transcriptomics at near-cellular resolution with Slide-seqV2. Nat. Biotechnol. *39*, 313–319. https://doi.org/10.1038/s41587-020-0739-1.
10. Borm, L.E., Mossi Albiach, A., Mannens, C.C.A., Janusauskas, J., Özgün, C., Fernández-García, D., Hodge, R., Castillo, F., Hedin, C.R.H., Villablanca, E.J., et al. (2023). Scalable in situ single-cell profiling by electrophoretic capture of mRNA using EEL FISH. Nat. Biotechnol. *41*, 222–231. https://doi.org/10.1038/s41587-022-01455-3.
11. Chen, X., Fischer, S., Zhang, A., Gillis, J., and Zador, A.M. (2022). Modular cell type organization of cortical areas revealed by in situ sequencing. Preprint at bioRxiv. https://doi.org/10.1101/2022.11.06.515380.
12. Zhang, M., Pan, X., Jung, W., Halpern, A.R., Eichhorn, S.W., Lei, Z., Cohen, L., Smith, K.A., Tasic, B., Yao, Z., et al. (2023). Molecularly defined and spatially resolved cell atlas of the whole mouse brain. Nature *624*, 343–354. https://doi.org/10.1038/s41586-023-06808-9.
13. Yao, Z., van Velthoven, C.T.J., Kunst, M., Zhang, M., McMillen, D., Lee, C., Jung, W., Goldy, J., Abdelhak, A., Aitken, M., et al. (2023). A high-resolution transcriptomic and spatial atlas of cell types in the whole mouse brain. Nature *624*, 317–332. https://doi.org/10.1038/s41586-023-06812-z.
14. Li, X., Du, Y., Huang, J.-F., Li, W.-W., Song, W., Fan, R.-N., Zhou, H., Jiang, T., Lu, C.-G., Guan, Z., et al. (2024). Link Brain-Wide Projectome

to Neuronal Dynamics in the Mouse Brain. Neurosci. Bull. *40*, 1621–1634. https://doi.org/10.1007/s12264-024-01232-z.

15. Ortiz, C., Navarro, J.F., Jurek, A., Märtin, A., Lundeberg, J., and Meletis, K. (2020). Molecular atlas of the adult mouse brain. Sci. Adv. *6*, eabb3446. https://doi.org/10.1126/sciadv.abb3446.
16. Shi, H., He, Y., Zhou, Y., Huang, J., Maher, K., Wang, B., Tang, Z., Luo, S., Tan, P., Wu, M., et al. (2023). Spatial atlas of the mouse central nervous system at molecular resolution. Nature *622*, 552–561. https://doi.org/10.1038/s41586-023-06569-5.
17. Langlieb, J., Sachdev, N.S., Balderrama, K.S., Nadaf, N.M., Raj, M., Murray, E., Webber, J.T., Vanderburg, C., Gazestani, V., Tward, D., et al. (2023). The molecular cytoarchitecture of the adult mouse brain. Nature *624*, 333–342. https://doi.org/10.1038/s41586-023-06818-7.
18. La Manno, G., Siletti, K., Furlan, A., Gyllborg, D., Vinsland, E., Mossi Albiach, A., Mattsson Langseth, C., Khven, I., Lederer, A.R., Dratva, L.M., et al. (2021). Molecular architecture of the developing mouse brain. Nature *596*, 92–96. https://doi.org/10.1038/s41586-021-03775-x.
19. Chen, A., Liao, S., Cheng, M., Ma, K., Wu, L., Lai, Y., Qiu, X., Yang, J., Xu, J., Hao, S., et al. (2022). Spatiotemporal transcriptomic atlas of mouse organogenesis using DNA nanoball-patterned arrays. Cell *185*, 1777–1792.e21. https://doi.org/10.1016/j.cell.2022.04.003.
20. Mattick, J.S., Amaral, P.P., Carninci, P., Carpenter, S., Chang, H.Y., Chen, L.-L., Chen, R., Dean, C., Dinger, M.E., Fitzgerald, K.A., et al. (2023). Long non-coding RNAs: definitions, functions, challenges and recommendations. Nat. Rev. Mol. Cell Biol. *24*, 430–447. https://doi.org/10.1038/s41580-022-00566-8.
21. Ang, C.E., Trevino, A.E., and Chang, H.Y. (2020). Diverse lncRNA mechanisms in brain development and disease. Curr. Opin. Genet. Dev. *65*, 42–46. https://doi.org/10.1016/j.gde.2020.05.006.
22. Andersen, R.E., Hong, S.J., Lim, J.J., Cui, M., Harpur, B.A., Hwang, E., Delgado, R.N., Ramos, A.D., Liu, S.J., Blencowe, B.J., et al. (2019). The Long Noncoding RNA Pnky Is a Trans-acting Regulator of Cortical Development In Vivo. Dev. Cell *49*, 632–642.e7. https://doi.org/10.1016/j.devcel.2019.04.032.
23. Feng, J., Bi, C., Clark, B.S., Mady, R., Shah, P., and Kohtz, J.D. (2006). The Evf-2 noncoding RNA is transcribed from the Dlx-5/6 ultraconserved region and functions as a Dlx-2 transcriptional coactivator. Genes Dev. *20*, 1470–1484. https://doi.org/10.1101/gad.1416106.
24. Liau, W.-S., Samaddar, S., Banerjee, S., and Bredy, T.W. (2021). On the functional relevance of spatiotemporally-specific patterns of experience-dependent long noncoding RNA expression in the brain. RNA Biol. *18*, 1025–1036. https://doi.org/10.1080/15476286.2020.1868165.
25. Kadakkuzha, B.M., Liu, X.-A., McCrate, J., Shankar, G., Rizzo, V., Afinogenova, A., Young, B., Fallahi, M., Carvalloza, A.C., Raveendra, B., et al. (2015). Transcriptome analyses of adult mouse brain reveal enrichment of lncRNAs in specific brain regions and neuronal populations. Front. Cell. Neurosci. *9*, 63. https://doi.org/10.3389/fncel.2015.00063.
26. Goff, L.A., Groff, A.F., Sauvageau, M., Trayes-Gibson, Z., Sanchez-Gomez, D.B., Morse, M., Martin, R.D., Elcavage, L.E., Liapis, S.C., Gonzalez-Celeiro, M., et al. (2015). Spatiotemporal expression and transcriptional perturbations by long noncoding RNAs in the mouse brain. Proc. Natl. Acad. Sci. USA *112*, 6855–6862. https://doi.org/10.1073/pnas.1411263112.
27. Wang, Q., Ding, S.-L., Li, Y., Royall, J., Feng, D., Lesnar, P., Graddis, N., Naeemi, M., Facer, B., Ho, A., et al. (2020). The Allen Mouse Brain Common Coordinate Framework: A 3D Reference Atlas. Cell *181*, 936–953.e20. https://doi.org/10.1016/j.cell.2020.04.007.
28. Yao, Z., van Velthoven, C.T.J., Nguyen, T.N., Goldy, J., Sedeno-Cortes, A.E., Baftizadeh, F., Bertagnolli, D., Casper, T., Chiang, M., Crichton, K., et al. (2021). A taxonomy of transcriptomic cell types across the isocortex and hippocampal formation. Cell *184*, 3222–3241.e26. https://doi.org/10.1016/j.cell.2021.04.021.
29. Shen, R., Liu, L., Wu, Z., Zhang, Y., Yuan, Z., Guo, J., Yang, F., Zhang, C., Chen, B., Feng, W., et al. (2022). Spatial-ID: a cell typing method for spatially resolved transcriptomics via transfer learning and spatial embedding. Nat. Commun. *13*, 7640. https://doi.org/10.1038/s41467-022-35288-0.
30. Liu, L., Zhang, Y., Niu, G., Li, Q., Li, Z., Zhu, T., Feng, C., Liu, X., Zhang, Y., Xu, T., et al. (2022). BrainBase: a curated knowledgebase for brain diseases. Nucleic Acids Res. *50*, D1131–D1138. https://doi.org/10.1093/nar/gkab987.
31. Bellenguez, C., Küçükali, F., Jansen, I.E., Kleineidam, L., Moreno-Grau, S., Amin, N., Naj, A.C., Campos-Martin, R., Grenier-Boley, B., Andrade, V., et al. (2022). New insights into the genetic etiology of Alzheimer's disease and related dementias. Nat. Genet. *54*, 412–436. https://doi.org/10.1038/s41588-022-01024-z.
32. Schizophrenia Working Group of the Psychiatric; Genomics Consortium (2014). Biological insights from 108 schizophrenia-associated genetic loci. Nature *511*, 421–427. https://doi.org/10.1038/nature13595.
33. Zingg, B., Hintiryan, H., Gou, L., Song, M.Y., Bay, M., Bienkowski, M.S., Foster, N.N., Yamashita, S., Bowman, I., Toga, A.W., et al. (2014). Neural networks of the mouse neocortex. Cell *156*, 1096–1111. https://doi.org/10.1016/j.cell.2014.02.023.
34. Pohlkamp, T., Dávid, C., Cauli, B., Gallopin, T., Bouché, E., Karagiannis, A., May, P., Herz, J., Frotscher, M., Staiger, J.F., et al. (2014). Characterization and distribution of Reelin-positive interneuron subtypes in the rat barrel cortex. Cereb. Cortex *24*, 3046–3058. https://doi.org/10.1093/cercor/bht161.
35. Kim, Y., Yang, G.R., Pradhan, K., Venkataraju, K.U., Bota, M., García Del Molino, L.C., Fitzgerald, G., Ram, K., He, M., Levine, J.M., et al. (2017). Brain-wide Maps Reveal Stereotyped Cell-Type-Based Cortical Architecture and Subcortical Sexual Dimorphism. Cell *171*, 456–469.e22. https://doi.org/10.1016/j.cell.2017.09.020.
36. Koirala, S., and Corfas, G. (2010). Identification of novel glial genes by single-cell transcriptional profiling of Bergmann glial cells from mouse cerebellum. PLoS One *5*, e9198. https://doi.org/10.1371/journal.pone.0009198.
37. Ramón-Cueto, A., and Avila, J. (1998). Olfactory ensheathing glia: properties and function. Brain Res. Bull. *46*, 175–187. https://doi.org/10.1016/s0361-9230(97)00463-2.
38. Higginson, J.R., and Barnett, S.C. (2011). The culture of olfactory ensheathing cells (OECs)—a distinct glial cell type. Exp. Neurol. *229*, 2–9. https://doi.org/10.1016/j.expneurol.2010.08.020.
39. Fearnley, J.M., and Lees, A.J. (1991). Ageing and Parkinson's disease: substantia nigra regional selectivity. Brain *114*, 2283–2301. https://doi.org/10.1093/brain/114.5.2283.
40. Niu, J., Zhong, Y., Jin, C., Cen, P., Wang, J., Cui, C., Xue, L., Cui, X., Tian, M., and Zhang, H. (2024). Positron Emission Tomography Imaging of Synaptic Dysfunction in Parkinson's Disease. Neurosci. Bull. *40*, 743–758. https://doi.org/10.1007/s12264-024-01188-0.
41. Nicholls, J.G., and Paton, J.F.R. (2009). Brainstem: neural networks vital for life. Philos. Trans. R. Soc. Lond. B Biol. Sci. *364*, 2447–2451. https://doi.org/10.1098/rstb.2009.0064.
42. Chen, J., Cai, M., and Zhan, C. (2024). Neuronal Regulation of Feeding and Energy Metabolism: A Focus on the Hypothalamus and Brainstem. Published online December 20, 2024. Neurosci. Bull. https://doi.org/10.1007/s12264-024-01335-7.
43. Sun, J., Yuan, Y., Wu, X., Liu, A., Wang, J., Yang, S., Liu, B., Kong, Y., Wang, L., Zhang, K., et al. (2022). Excitatory SST neurons in the medial paralemniscal nucleus control repetitive self-grooming and encode reward. Neuron *110*, 3356–3373.e8. https://doi.org/10.1016/j.neuron.2022.08.010.
44. Zhao, E., Stone, M.R., Ren, X., Guenthoer, J., Smythe, K.S., Pulliam, T., Williams, S.R., Uytingco, C.R., Taylor, S.E.B., Nghiem, P., et al. (2021).

Spatial transcriptomics at subspot resolution with BayesSpace. Nat. Biotechnol. *39*, 1375–1384. https://doi.org/10.1038/s41587-021-00935-2.

45. DeTomaso, D., and Yosef, N. (2021). Hotspot identifies informative gene modules across modalities of single-cell genomics. Cell Syst. *12*, 446–456.e9. https://doi.org/10.1016/j.cels.2021.04.005.
46. Pinault, D. (2004). The thalamic reticular nucleus: structure, function and concept. Brain Res. Brain Res. Rev. *46*, 1–31. https://doi.org/10.1016/j.brainresrev.2004.04.008.
47. Steullet, P., Cabungcal, J.H., Bukhari, S.A., Ardelt, M.I., Pantazopoulos, H., Hamati, F., Salt, T.E., Cuenod, M., Do, K.Q., and Berretta, S. (2018). The thalamic reticular nucleus in schizophrenia and bipolar disorder: role of parvalbumin-expressing neuron networks and oxidative stress. Mol. Psychiatry *23*, 2057–2065. https://doi.org/10.1038/mp.2017.230.
48. Shi, Y., Huang, L., Dong, H., Yang, M., Ding, W., Zhou, X., Lu, T., Liu, Z., Zhou, X., Wang, M., et al. (2024). Decoding the spatiotemporal regulation of transcription factors during human spinal cord development. Cell Res. *34*, 193–213. https://doi.org/10.1038/s41422-023-00897-x.
49. Abe, K. (2024). Dynamic activity changes in transcription factors: Unlocking the mechanisms regulating physiological changes in the brain. Published online August 10, 2024. Neurosci. Res. https://doi.org/10.1016/j.neures.2024.08.001.
50. Loupe, J.M., Anderson, A.G., Rizzardi, L.F., Rodriguez-Nunez, I., Moyers, B., Trausch-Lowther, K., Jain, R., Bunney, W.E., Bunney, B.G., Cartagena, P., et al. (2024). Multiomic profiling of transcription factor binding and function in human brain. Nat. Neurosci. *27*, 1387–1399. https://doi.org/10.1038/s41593-024-01658-8.
51. Cheng, M., Wu, L., Han, L., Huang, X., Lai, Y., Xu, J., Wang, S., Li, M., Zheng, H., Feng, W., et al. (2022). A Cellular Resolution Spatial Transcriptomic Landscape of the Medial Structures in Postnatal Mouse Brain. Front. Cell Dev. Biol. *10*, 878346. https://doi.org/10.3389/fcell.2022.878346.
52. Aibar, S., González-Blas, C.B., Moerman, T., Huynh-Thu, V.A., Imrichova, H., Hulselmans, G., Rambow, F., Marine, J.-C., Geurts, P., Aerts, J., et al. (2017). SCENIC: single-cell regulatory network inference and clustering. Nat. Methods *14*, 1083–1086. https://doi.org/10.1038/nmeth.4463.
53. Lambert, S.A., Jolma, A., Campitelli, L.F., Das, P.K., Yin, Y., Albu, M., Chen, X., Taipale, J., Hughes, T.R., and Weirauch, M.T. (2018). The Human Transcription Factors. Cell *172*, 650–665. https://doi.org/10.1016/j.cell.2018.01.029.
54. Li, Y., Li, Z., Wang, C., Yang, M., He, Z., Wang, F., Zhang, Y., Li, R., Gong, Y., Wang, B., et al. (2023). Spatiotemporal transcriptome atlas reveals the regional specification of the developing human brain. Cell *186*, 5892–5909.e22. https://doi.org/10.1016/j.cell.2023.11.016.
55. Waclaw, R.R., Ehrman, L.A., Merchan-Sala, P., Kohli, V., Nardini, D., and Campbell, K. (2017). Foxo1 is a downstream effector of Isl1 in direct pathway striatal projection neuron development within the embryonic mouse telencephalon. Mol. Cell. Neurosci. *80*, 44–51. https://doi.org/10.1016/j.mcn.2017.02.003.
56. Cadwell, C.R., Bhaduri, A., Mostajo-Radji, M.A., Keefe, M.G., and Nowakowski, T.J. (2019). Development and Arealization of the Cerebral Cortex. Neuron *103*, 980–1004. https://doi.org/10.1016/j.neuron.2019.07.009.
57. Qiu, X., Zhu, D.Y., Lu, Y., Yao, J., Jing, Z., Min, K.H., Cheng, M., Pan, H., Zuo, L., King, S., et al. (2024). Spatiotemporal modeling of molecular holograms. Cell *187*, 7351–7373.e61. https://doi.org/10.1016/j.cell.2024.10.011.
58. Hevner, R.F., Shi, L., Justice, N., Hsueh, Y., Sheng, M., Smiga, S., Bulfone, A., Goffinet, A.M., Campagnoni, A.T., and Rubenstein, J.L. (2001). Tbr1 regulates differentiation of the preplate and layer 6. Neuron *29*, 353–366. https://doi.org/10.1016/s0896-6273(01)00211-2.
59. Bedogni, F., Hodge, R.D., Elsen, G.E., Nelson, B.R., Daza, R.A.M., Beyer, R.P., Bammler, T.K., Rubenstein, J.L.R., and Hevner, R.F. (2010). Tbr1 regulates regional and laminar identity of postmitotic neurons in developing neocortex. Proc. Natl. Acad. Sci. USA *107*, 13129–13134. https://doi.org/10.1073/pnas.1002285107.
60. Shi, Y., Chichung Lie, D., Taupin, P., Nakashima, K., Ray, J., Yu, R.T., Gage, F.H., and Evans, R.M. (2004). Expression and function of orphan nuclear receptor TLX in adult neural stem cells. Nature *427*, 78–83. https://doi.org/10.1038/nature02211.
61. Schmouth, J.-F., Arenillas, D., Corso-Díaz, X., Xie, Y.-Y., Bohacec, S., Banks, K.G., Bonaguro, R.J., Wong, S.H., Jones, S.J.M., Marra, M.A., et al. (2015). Combined serial analysis of gene expression and transcription factor binding site prediction identifies novel-candidate-target genes of Nr2e1 in neocortex development. BMC Genomics *16*, 545. https://doi.org/10.1186/s12864-015-1770-3.
62. Land, P.W., and Monaghan, A.P. (2003). Expression of the transcription factor, tailless, is required for formation of superficial cortical layers. Cereb. Cortex *13*, 921–931. https://doi.org/10.1093/cercor/13.9.921.
63. Shetty, A.S., Godbole, G., Maheshwari, U., Padmanabhan, H., Chaudhary, R., Muralidharan, B., Hou, P.-S., Monuki, E.S., Kuo, H.-C., Rema, V., et al. (2013). Lhx2 regulates a cortex-specific mechanism for barrel formation. Proc. Natl. Acad. Sci. USA *110*, E4913–E4921. https://doi.org/10.1073/pnas.1311158110.
64. de Juan Romero, C., Bruder, C., Tomasello, U., Sanz-Anquela, J.M., and Borrell, V. (2015). Discrete domains of gene expression in germinal layers distinguish the development of gyrencephaly. EMBO J. *34*, 1859–1874. https://doi.org/10.15252/embj.201591176.
65. Erzurumlu, R.S., and Gaspar, P. (2012). Development and critical period plasticity of the barrel cortex. Eur. J. Neurosci. *35*, 1540–1553. https://doi.org/10.1111/j.1460-9568.2012.08075.x.
66. Braun, E., Danan-Gotthold, M., Borm, L.E., Lee, K.W., Vinsland, E., Lönnerberg, P., Hu, L., Li, X., He, X., Andrusivová, Ž., et al. (2023). Comprehensive cell atlas of the first-trimester developing human brain. Science *382*, eadf1226. https://doi.org/10.1126/science.adf1226.
67. Guennewig, B., and Cooper, A.A. (2014). The central role of noncoding RNA in the brain. Int. Rev. Neurobiol. *116*, 153–194. https://doi.org/10.1016/B978-0-12-801105-8.00007-2.
68. Mercer, T.R., Dinger, M.E., Sunkin, S.M., Mehler, M.F., and Mattick, J.S. (2008). Specific expression of long noncoding RNAs in the mouse brain. Proc. Natl. Acad. Sci. USA *105*, 716–721. https://doi.org/10.1073/pnas.0706729105.
69. Salvatori, B., Biscarini, S., and Morlando, M. (2020). Non-coding RNAs in Nervous System Development and Disease. Front. Cell Dev. Biol. *8*, 273. https://doi.org/10.3389/fcell.2020.00273.
70. Qureshi, I.A., and Mehler, M.F. (2012). Emerging roles of non-coding RNAs in brain evolution, development, plasticity and disease. Nat. Rev. Neurosci. *13*, 528–541. https://doi.org/10.1038/nrn3234.
71. Srinivas, T., Mathias, C., Oliveira-Mateos, C., and Guil, S. (2023). Roles of lncRNAs in brain development and pathogenesis: Emerging therapeutic opportunities. Mol. Ther. *31*, 1550–1561. https://doi.org/10.1016/j.ymthe.2023.02.008.
72. Li, W., Shen, W., Zhang, B., Tian, K., Li, Y., Mu, L., Luo, Z., Zhong, X., Wu, X., Liu, Y., et al. (2020). Long non-coding RNA LncKdm2b regulates cortical neuronal differentiation by cis-activating Kdm2b. Protein Cell *11*, 161–186. https://doi.org/10.1007/s13238-019-0650-z.
73. Joshi, P.D. (2019). Molecular Characterization and Functional Analysis of a Novel Long Noncoding RNA in the Mouse. PhD thesis (Georg-August-Universität Göttingen).
74. Wang, F., Wang, Q., Liu, B., Mei, L., Ma, S., Wang, S., Wang, R., Zhang, Y., Niu, C., Xiong, Z., et al. (2021). The long noncoding RNA Synage regulates synapse stability and neuronal function in the cerebellum. Cell Death Differ. *28*, 2634–2650. https://doi.org/10.1038/s41418-021-00774-3.
75. Jin, Y., Zhang, B., Lu, J., Song, Y., Wang, W., Zhang, W., Shao, F., Gong, M., Wang, M., Liang, X., et al. (2021). Long noncoding RNA PM maintains cerebellar synaptic integrity and Cbln1 activation via Pax6/Mll1-mediated

H3K4me3. PLoS Biol. *19*, e3001297. https://doi.org/10.1371/journal.pbio.3001297.

76. Yue, Y., Zhang, W., Liu, C., Niu, Y., and Tong, W. (2015). Long non-coding RNA Gm15577 is involved in mouse cerebellar neurogenesis. Zhonghua Bing Li Xue Za Zhi *44*, 504–508.
77. Liu, C., Li, R., Li, Y., Lin, X., Zhao, K., Liu, Q., Wang, S., Yang, X., Shi, X., Ma, Y., et al. (2022). Spatiotemporal mapping of gene expression landscapes and developmental trajectories during zebrafish embryogenesis. Dev. Cell *57*, 1284–1298.e5. https://doi.org/10.1016/j.devcel.2022.04.009.
78. Sigova, A.A., Mullen, A.C., Molinie, B., Gupta, S., Orlando, D.A., Guenther, M.G., Almada, A.E., Lin, C., Sharp, P.A., Giallourakis, C.C., et al. (2013). Divergent transcription of long noncoding RNA/mRNA gene pairs in embryonic stem cells. Proc. Natl. Acad. Sci. USA *110*, 2876–2881. https://doi.org/10.1073/pnas.1221904110.
79. Wu, X., and Sharp, P.A. (2013). Divergent transcription: a driving force for new gene origination? Cell *155*, 990–996. https://doi.org/10.1016/j.cell.2013.10.048.
80. Sjöstedt, E., Fagerberg, L., Hallström, B.M., Häggmark, A., Mitsios, N., Nilsson, P., Pontén, F., Hökfelt, T., Uhlén, M., and Mulder, J. (2015). Defining the Human Brain Proteome Using Transcriptomics and Antibody-Based Profiling with a Focus on the Cerebral Cortex. PLoS One *10*, e0130028. https://doi.org/10.1371/journal.pone.0130028.
81. Schmitz, S.U., Grote, P., and Herrmann, B.G. (2016). Mechanisms of long noncoding RNA function in development and disease. Cell. Mol. Life Sci. *73*, 2491–2509. https://doi.org/10.1007/s00018-016-2174-5.
82. Hamazaki, N., Uesaka, M., Nakashima, K., Agata, K., and Imamura, T. (2015). Gene activation-associated long noncoding RNAs function in mouse preimplantation development. Development *142*, 910–920. https://doi.org/10.1242/dev.116996.
83. Alexander, L., Clarke, H.F., and Roberts, A.C. (2019). A focus on the functions of area 25. Brain Sci. *9*, 129. https://doi.org/10.3390/brainsci9060129.
84. Chen, A., Sun, Y., Lei, Y., Li, C., Liao, S., Meng, J., Bai, Y., Liu, Z., Liang, Z., Zhu, Z., et al. (2023). Single-cell spatial transcriptome reveals cell-type organization in the macaque cortex. Cell *186*, 3726–3743.e24. https://doi.org/10.1016/j.cell.2023.06.009.
85. Bach, E.C., and Kandler, K. (2021). Author Correction: long-term potentiation of glycinergic synapses by semi-natural stimulation patterns during tonotopic map refinement. Sci. Rep. *11*, 22022. https://doi.org/10.1038/s41598-021-01422-z.
86. Moore, A.K., and Wehr, M. (2013). Parvalbumin-expressing inhibitory interneurons in auditory cortex are well-tuned for frequency. J. Neurosci. *33*, 13713–13723. https://doi.org/10.1523/JNEUROSCI.0663-13.2013.
87. Nocon, J.C., Gritton, H.J., James, N.M., Mount, R.A., Qu, Z., Han, X., and Sen, K. (2023). Parvalbumin neurons enhance temporal coding and reduce cortical noise in complex auditory scenes. Commun. Biol. *6*, 751. https://doi.org/10.1038/s42003-023-05126-0.
88. Ng, L., Bernard, A., Lau, C., Overly, C.C., Dong, H.-W., Kuan, C., Pathak, S., Sunkin, S.M., Dang, C., Bohland, J.W., et al. (2009). An anatomic gene expression atlas of the adult mouse brain. Nat. Neurosci. *12*, 356–362. https://doi.org/10.1038/nn.2281.
89. Jafri, A., Belkadi, A., Zaidi, S.I.A., Getsy, P., Wilson, C.G., and Martin, R.J. (2013). Lung inflammation induces IL-1β expression in hypoglossal neurons in rat brainstem. Respir. Physiol. Neurobiol. *188*, 21–28. https://doi.org/10.1016/j.resp.2013.04.022.
90. Lavezzi, A.M., Corna, M., Mingrone, R., and Matturri, L. (2010). Study of the human hypoglossal nucleus: normal development and morpho-functional alterations in sudden unexplained late fetal and infant death. Brain Dev. *32*, 275–284. https://doi.org/10.1016/j.braindev.2009.05.006.
91. Swanson, L.W. (2012). Brain Architecture: Understanding the Basic Plan (OUP).
92. Paxinos, G. (2014). The Rat Nervous System (Academic Press).
93. Chou, S.-J., Perez-Garcia, C.G., Kroll, T.T., and O'Leary, D.D.M. (2009). Lhx2 specifies regional fate in Emx1 lineage of telencephalic progenitors generating cerebral cortex. Nat. Neurosci. *12*, 1381–1389. https://doi.org/10.1038/nn.2427.
94. Hao, Y., Hao, S., Andersen-Nissen, E., Mauck, W.M., 3rd, Zheng, S., Butler, A., Lee, M.J., Wilk, A.J., Darby, C., Zager, M., et al. (2021). Integrated analysis of multimodal single-cell data. Cell *184*, 3573–3587.e29. https://doi.org/10.1016/j.cell.2021.04.048.
95. Liaw, A., and Wiener, M. (2002). Classification and Regression by randomForest. R News *2*, 18–22. https://CRAN.R-project.org/doc/Rnews/.
96. Korsunsky, I., Millard, N., Fan, J., Slowikowski, K., Zhang, F., Wei, K., Baglaenko, Y., Brenner, M., Loh, P.-R., and Raychaudhuri, S. (2019). Fast, sensitive and accurate integration of single-cell data with Harmony. Nat. Methods *16*, 1289–1296. https://doi.org/10.1038/s41592-019-0619-0.
97. Wickham, H., Averick, M., Bryan, J., Chang, W., McGowan, L.D., François, R., Grolemund, G., Hayes, A., Henry, L., Hester, J., et al. (2019). Welcome to the Tidyverse. J. Open Source Software *4*, 1686. https://doi.org/10.21105/joss.01686.
98. Wickham, H. (2016). Data Analysis. In ggplot2 (Springer), pp. 189–201. https://doi.org/10.1007/978-3-319-24277-4_9.
99. Paszke, A., Gross, S., Massa, F., Lerer, A., Bradbury, J., Chanan, G., Killeen, T., Lin, Z., Gimelshein, N., Antiga, L., et al. (2019). PyTorch: An Imperative Style, High-Performance Deep Learning Library. Advances in Neural Information Processing Systems 32 (NeurIPS 2019).
100. Fey, M., and Lenssen, J.E. (2019). Fast Graph Representation Learning with PyTorch Geometric. Preprint at arXiv.
101. Harris, C.R., Millman, K.J., van der Walt, S.J., Gommers, R., Virtanen, P., Cournapeau, D., Wieser, E., Taylor, J., Berg, S., Smith, N.J., et al. (2020). Array programming with NumPy. Nature *585*, 357–362. https://doi.org/10.1038/s41586-020-2649-2.
102. McKinney, W. (2017). Python for Data Analysis: Data Wrangling with Pandas, NumPy, and IPython (O'Reilly Media, Inc.).
103. Wolf, F.A., Angerer, P., and Theis, F.J. (2018). SCANPY: large-scale single-cell gene expression data analysis. Genome Biol. *19*, 15. https://doi.org/10.1186/s13059-017-1382-0.
104. Jing, Z., Zhu, Q., Li, L., Xie, Y., Wu, X., Fang, Q., Yang, B., Dai, B., Xu, X., Pan, H., et al. (2024). Spaco: A comprehensive tool for coloring spatial data at single-cell resolution. Patterns (N Y) *5*, 100915. https://doi.org/10.1016/j.patter.2023.100915.
105. Yu, G., Wang, L.-G., Han, Y., and He, Q.-Y. (2012). clusterProfiler: an R package for comparing biological themes among gene clusters. Omics *16*, 284–287. https://doi.org/10.1089/omi.2011.0118.
106. Hunter, J.D. (2007). Matplotlib: A 2D Graphics Environment. Comput. Sci. Eng. *9*, 90–95. https://doi.org/10.1109/MCSE.2007.55.
107. Virshup, I., Rybakov, S., Theis, F.J., Angerer, P., and Wolf, F.A. (2024). anndata: Access and store annotated data matrices. J. Open Source Software *9*, 4371. https://doi.org/10.21105/joss.04371.
108. Dobin, A., Davis, C.A., Schlesinger, F., Drenkow, J., Zaleski, C., Jha, S., Batut, P., Chaisson, M., and Gingeras, T.R. (2013). STAR: ultrafast universal RNA-seq aligner. Bioinformatics *29*, 15–21. https://doi.org/10.1093/bioinformatics/bts635.
109. Li, M., Liu, H., Li, M., Fang, S., Kang, Q., Zhang, J., Teng, F., Wang, D., Cen, W., Li, Z., et al. (2023). StereoCell enables high accuracy single cell segmentation for spatial transcriptomic dataset. Prepirnt at. bioRxiv. https://doi.org/10.1101/2023.02.28.530414.
110. Zhang, Z., Liu, Q., and Wang, Y. (2018). Road Extraction by Deep Residual U-Net. IEEE Geosci. Remote Sens. Lett. *15*, 749–753. https://doi.org/10.1109/LGRS.2018.2802944.
111. Jing, Z., Yang, B., and Bai, Y. (2024). Protocol for enhancing visualization clarity for categorical spatial datasets using Spaco. Star Protoc. *5*, 103062. https://doi.org/10.1016/j.xpro.2024.103062.

112. Bakken, T.E., Hodge, R.D., Miller, J.A., Yao, Z., Nguyen, T.N., Aevermann, B., Barkan, E., Bertagnolli, D., Casper, T., Dee, N., et al. (2018). Single-nucleus and single-cell transcriptomes compared in matched cortical cell types. PLoS One *13*, e0209648. https://doi.org/10.1371/journal.pone.0209648.

113. Van de Sande, B., Flerin, C., Davie, K., De Waegeneer, M., Hulselmans, G., Aibar, S., Seurinck, R., Saelens, W., Cannoodt, R., Rouchon, Q., et al. (2020). A scalable SCENIC workflow for single-cell gene regulatory network analysis. Nat. Protoc. *15*, 2247–2276. https://doi.org/10.1038/s41596-020-0336-2.

114. Huynh-Thu, V.A., Irrthum, A., Wehenkel, L., and Geurts, P. (2010). Inferring regulatory networks from expression data using tree-based methods. PLoS One *5*, e12776. https://doi.org/10.1371/journal.pone.0012776.

115. Qiu, X., Zhang, Y., Martin-Rufino, J.D., Weng, C., Hosseinzadeh, S., Yang, D., Pogson, A.N., Hein, M.Y., Hoi Joseph Min, K., Wang, L., et al. (2022). Mapping transcriptomic vector fields of single cells. Cell *185*, 690–711.e45. https://doi.org/10.1016/j.cell.2021.12.045.

116. Fabian, P. (2011). Scikit-learn: Machine learning in Python. J. Mach. Learn. Res. *12*, 2825.

117. Zerbino, D.R., Achuthan, P., Akanni, W., Amode, M.R., Barrell, D., Bhai, J., Billis, K., Cummins, C., Gall, A., Girón, C.G., et al. (2018). Ensembl 2018. Nucleic Acids Res. *46*, D754–D761. https://doi.org/10.1093/nar/gkx1098.

STAR★METHODS

KEY RESOURCES TABLE

REAGENT or RESOURCE	SOURCE	IDENTIFIER
Chemicals, peptides, and recombinant proteins		
Tissue-Tek OCT	Sakura	Cat# 4583; RRID: SCR_026577
Methanol	Sigma	Cat# 34860; RRID: SCR_026579
ssDNA reagent	Invitrogen	Cat# Q10212; RRID: SCR_026580
20 × SSC	Ambion	Cat# AM9770; RRID: SCR_026581
Pepsin	Sigma	Cat# P7000; RRID: SCR_026582
RNase inhibitor	NEB	Cat# M0314L; RRID: SCR_026583
Exonuclease I	NEB	Cat# M0293L; RRID: SCR_026584
KAPA HiFi Hotstart Ready Mix	Roche	Cat# KK2602; RRID: SCR_026585
Qubit dsDNA HS Assay Kit	Invitrogen	Cat# Q32854; RRID: SCR_026586
VAHTS DNA Clean Beads	Vazyme	Cat# N411-03; RRID: SCR_026588
Deposited data		
Raw data of Stereo-seq and snRNA-seq data	This study	CNGB: CNP0003837 (https://db.cngb.org/search/?q=CNP0003837)
Processed data of Stereo-seq and snRNA-seq data	This study	https://doi.org/10.12412/BSDC.1699433096.20001
Public scRNA-seq data of mouse isocortex and hippocampal formation	Yao et al.[28]	https://assets.nemoarchive.org/dat-jb2f34y
Public scRNA-seq data of mouse nervous system	Zeisel et al.[3]	http://mousebrain.org/adolescent
Public Stereo-seq data of E12.5, E14.5, E16.5 mouse brain	Chen et al.[19]	https://db.cngb.org/stomics/mosta
Public Stereo-seq data of P7 mouse brain	Cheng et al.[51]	https://db.cngb.org/stomics/datasets/STDS0000139/data
Experimental models: Organisms/strains		
Mouse: C57BL/6, Male	Shanghai Lingchang Biotechnology Co., Ltd.	N/A
Oligonucleotides		
Stereo-seq-TSO: CTGCTGACGTA CTGAGAGGC/rG//rG//iXNA_G/	Sangon	N/A
cDNA PCR primer: CTGCTGACGTA CTGAGAGGC	Sangon	N/A
Stereo-seq-library-F: /5phos/CTGCT GACGTACTGAGAGG*C*A	Sangon	N/A
Stereo-seq-library-R: GAGACGTTCT CGACTCAGCAGA	Sangon	N/A
Stereo-seq-library-splint-oligo: GTACGT CAGCAGGAGACGTTCTCG	Sangon	N/A
Stereo-seq-read1: CTGCTGACGTAC TGAGAGGCATGGCGACCTTATCAG	Sangon	N/A
Stereo-seq-MDA-primer:TCTGCTGA GTCGAGAACGTC	Sangon	N/A
Stereo-seq-read2: GCCATGTCGTTCTG TGAGCCAAGGAGTT	Sangon	N/A
Software and algorithms		
R v4.1 and greater	R Foundation	https://cran.r-project.org
Seurat v4.3.0 and greater	Hao et al.[94]	https://satijalab.org/seurat

(*Continued on next page*)

Continued

REAGENT or RESOURCE	SOURCE	IDENTIFIER
SeuratDisk v0.0.0.9020	Satija Lab	https://github.com/mojaveazure/seurat-disk
Spatial-ID	Shen et al.[29]	https://github.com/TencentAILabHealthcare/spatialID
randomForest v4.7-1.1	Liaw and Wiener[95]	https://cran.r-project.org/web/packages/randomForest/index.html
harmony v0.1	Korsunsky et al.[96]	https://github.com/eddelbuettel/harmony
scrattch.hicat v1.0.0	Allen Institute	https://github.com/AllenInstitute/scrattch.hicat
tidyverse v1.3.2	Wickham et al.[97]	https://cran.r-project.org/web/packages/tidyverse/index.html
ggplot2 v3.4.1	Wickham[98]	https://cran.r-project.org/web/packages/ggplot2/index.html
python v3.8 and greater	Python Software Foundation	https://www.python.org
PyTorch v1.13.1	Paszke et al.[99]	https://pytorch.org
PyTorch Geometric v2.1.0	Fey and Lenssen[100]	https://pytorch-geometric.readthedocs.io
numpy v1.23.3	Harris et al.[101]	https://numpy.org
pandas v1.5.0	McKinney[102]	https://pandas.pydata.org
scanpy v1.9.1	Wolf et al.[103]	https://scanpy.readthedocs.io
Spateo v1.1.0	Qiu et al.[57]	https://github.com/aristoteleo/spateo-release
Spaco v0.2.2	Jing et al.[104]	https://pypi.org/project/spaco-release/
SCENIC v1.1.2	Aibar et al.[52]	https://scenic.aertslab.org/
Hotspot v0.9.0	DeTomaso and Yosef[45]	https://yoseflab.github.io/Hotspot/
BayesSpace v1.5.1	Zhao et al.[44]	https://github.com/edward130603/BayesSpace
clusterprofiler v3.2	Yu et al.[105]	https://bioconductor.org/packages/release/bioc/html/clusterProfiler.html
matplotlib v3.8.3	Hunter[106]	https://matplotlib.org/
anndata v0.8.0	Virshup et al.[107]	https://anndata.readthedocs.io/
loompy v3.0	Linnarsson Lab	https://github.com/linnarsson-lab/loompy

EXPERIMENTAL MODEL AND STUDY PARTICIPANT DETAILS

Animals

Animal protocol was approved (NA-005-2022) by the Biomedical Research Ethics Committee of CAS Center for Excellence in Brain Science and Intelligence Technology, Chinese Academy of Sciences. Animal care complied with the guideline of this committee. Mouse brains were collected from P1, P14 and 11-week-old C57BL/6J male mice. Left hemispheres were collected from these male mice for experiments.

METHOD DETAILS

Brain tissue collection for Stereo-seq

Male mice (C57BL/6J) were used for the experiments. Left hemispheres of male mice (P1, P14, 11 weeks) were collected. Animals were deeply anesthetized with 3% isoflurane and quickly perfused with 4°C bubbled (with a mixture of 95% O_2 and 5% CO_2) artificial cerebrospinal fluid (ACSF, containing (in mM) NaCl 126, KCl 2.5, NaH_2PO_4 1.25, $MgCl_2$ 2, $CaCl_2$ 2, $NaHCO_3$ 26, and glucose 10, 300–305 mOsm). After the dissection of the brain, the whole left hemisphere was obtained using the mouse brain sections (RWD, #68708). To prevent the formation of ice crystals during the tissue freezing, ACSF on the surface of brain blocks were dried with sterile gauze and brain blocks were transferred into OCT (4583#, Sakura) for 3 times to adequately displace the remaining ACSF. Subsequently, brain blocks were transferred to a self-made metal mold filled with OCT and quickly frozen with dry ice. After the freezing, brain blocks were stored in -80°C before the slicing. To minimize the RNA degradation, all solutions we used were prepared with diethyl

Please cite this article in press as: Han et al., Single-cell spatial transcriptomic atlas of the whole mouse brain, Neuron (2025), https://doi.org/10.1016/j.neuron.2025.02.015

pyrocarbonate (DEPC) (B501005-0005, Sangon Biotech) treated sterilized water (DEPC-H_2O), and all instruments were washed with DEPC-H_2O and RNase Zap (AM9780, Invitrogen). And time spent for the whole tissue collection process was limited to 10 min.

Tissue cryosection, section flattening and RNA quality control

Cryosection was performed to obtain 10-μm sections for Stereo-seq at 100-μm interval in coronal coordinate. The sections were carefully placed on pre-cooled Stereo-seq chips (-20°C) with a finger gently pressed under the chip to gradually raise section temperature on Stereo-seq chip, which helps to reduce bubbles and wrinkles. RNA quality was examined, and only samples with RNA integrity number (RIN) value greater than or equal to 9 were used for analysis.

Stereo-seq experiment procedure

The tissue section on the Stereo-seq chip (1 cm x 1 cm) was then incubated at 37°C for 3 min and subsequently fixed in methanol (Sigma, 34860; precooled for 20 min at -20°C; 1 ml methanol was added in multi-orifice for each section) and incubated at -20°C for 30 min. Methanol was then dried out in a hood. Tissue section on the chip was then stained with ssDNA reagent (Invitrogen, Q10212) for 5 min and subsequently washed with 0.1x SSC buffer (Ambion, AM9770; containing 0.05 U/μl RNase inhibitor). Section images were captured using Zeiss Axio Scan Z1 microscope (at EGFP and DAPI wavelength, 10-ms exposure). Tissue sections were then permeated by incubating in 0.1% pepsin (Sigma, P7000, pepsin was prewarmed at 37°C for 3 min) at 37°C for 12 min (6 min for olfactory bulb) in 0.01 M HCl buffer (pH = 2) and then washed with 0.1x SSC buffer (containing 0.05 U/μl RNase inhibitor) to remove pepsin. In this step, RNAs were released from the permeated tissue and captured by the Stereo-seq chip. RNAs were then reverse transcribed for 1 hour at 42°C. After reverse transcription, tissue sections were washed with 0.1x SSC buffer and digested with tissue removal buffer (10 mM Tris-HCl, 25 mM EDTA, 100 mM NaCl, 0.5% SDS) at 37°C for 30 min, and then the chips were washed twice with 0.1x SSC buffer. The cDNA-containing chips were then subjected to Exonuclease I (NEB, M0293L) treatment for 3 hours at 55°C. The released cDNAs were collected and the chips were washed once with NF-water. The cDNAs were purified using 0.8x VAHTS™ DNA Clean Beads and then amplified with Hot Start DNA Polymerase (QIAGEN). The PCR reaction protocol was: first incubation at 95°C for 5 min, 15 cycles at 98°C for 20 s, 58°C for 20 s, 72°C for 3 min and a final incubation at 72°C for 5 min. The PCR products were then purified using 0.6x VAHTS™ DNA Clean Beads and were quantified by Qubit dsDNA HS Assay kit (Invitrogen, Q32854).

Stereo-seq library construction and sequencing

20 ng of cDNA products were fragmented using in-house Tn5 transposase at 55°C for 10 min, after which the reaction was stopped by the addition of 0.02% SDS. The fragmentation products were added with KAPA HiFi Hotstart Ready Mix (Roche, KK2602), 0.3 μM Stereo-seq-Library-F primer and 0.3 μM Stereo-seq-Library-R, and the samples were then transferred to a thermal cycler and for amplification using the following protocol: 1 cycle at 95°C for 5 min, 13 cycles at 98°C for 20 s, 58°C for 20 s, and 72°C for 30 s, and 1 cycle at 72°C for 5 min. The PCR products were then purified using VAHTS™ DNA Clean Beads (0.6x and 0.15x). Finally, the library was sequenced on MGI DNBSEQ™ T10 sequencer with sequencing length of 35 bp for read 1 and 100 bp for read 2.

Processing of Stereo-seq raw data

The stereo-seq libraries were sequenced by MGI DNBSEQ™ T10 sequencer, and the fastq files generated were then processed with the SAW pipeline (https://github.com/BGIResearch/SAW). For read 1, coordination identity (CID) sequences were mapped to the designed coordinates of the *in situ* captured chip, allowing 1 base mismatch. Unique molecular identifiers (UMI) having either N bases or more than 2 bases with quality score less than 10 were filtered out. The associated CIDs and UMIs extracted from read 1 were appended to the read header of relative read 2. Then STAR[108] was used to align retained read 2 to reference genome (mm10), and mapped reads with MAPQ >10 were kept. UMIs with the same CID and the same gene locus were collapsed, where one mismatch was allowed for sequencing and PCR errors. Finally, this information was used to generate an expression profile matrix containing coordinates.

Quality control of Stereo-seq sections

For brain section quality, we manually checked the boundary of each brain section generated by Stereo-seq data, there were 7 sections removed due to abnormal capture of transcripts as compared with their adjacent sections, which may be caused by incomplete attachment of brain tissue to the chips. For the rest of 200 sections, we then identified and filtered out low-quality brain sections with less than 1000 genes based on the distribution of average gene numbers of sections on bin100. Accordingly, 5 low quality sections were excluded. Totally, 12 brain sections were excluded, the rest of 195 sections (123 sections for mouse #1, 72 sections for mouse #2) were used for analysis.

To assess batch effects, we divided the 123 brain sections from Mouse #1 into 12 groups, based on the time intervals corresponding to the appearance and disappearance of major brain regions. Data from each group of sections were integrated and subjected to unsupervised clustering. Using PCA and UMAP for dimensionality reduction, we observed that the clusters within each group were evenly distributed across the brain sections, indicating no significant batch effects (Figure S1). Moreover, the spatial distribution of each cluster across the sections showed a high degree of consistency in spatial localization, as exemplified by the T37-T47 group (Figure S1).

Please cite this article in press as: Han et al., Single-cell spatial transcriptomic atlas of the whole mouse brain, Neuron (2025), https://doi.org/10.1016/j.neuron.2025.02.015

Cell segmentation

We harmonize the nucleic acid staining image and CID-containing expression matrix from the same section to perform spatial cell segmentation. Specifically, we utilized StereoCell (https://github.com/BGIResearch/StereoCell)[109] to perform a three-step cell segmentation procedure. Firstly, staining images were registered with their corresponding expression matrices. Secondly, cell morphological segmentation was done based on nuclei-stained images. We employed median filtering to smooth the noise that may present in input staining images. Then, a modified U-Net based deep learning model[110] was used to identify cell morphology from the image. Cells were filtered by their area, while shape and boundary was revised using opening operation (erode and dilate). Thirdly, after the basic nuclei mask was identified, a molecule labeling step is employed to label spatially detected UMIs to cells. The UMI that are contained within each nucleus are assigned directly to each cell. Then, to retrieve the UMIs in cytoplasm, a Gaussian mixture model was used to estimate the probability of each remaining UMI belonging to a given cell based on the initial nuclei segmentation, and label the UMIs with high confidence to the corresponding cells. Finally, we aggregated the UMIs that belong to the same cell, for each gene, and generated a cell-gene matrix for downstream analysis.

Gene-based brain region parcellation

Firstly, the expression profile matrix of both the coronal and sagittal mouse brain was divided into non-overlapping bins covering an area of 100 ×100 DNB (i.e., Bin100 spots). The UMIs were aggregated per gene within each bin. The resulting bins were further processed by Seurat.[94] To be specific, we performed quality control on the Bin100 spots of each brain section, filtering out bins with gene counts less than 200 and mitochondrial proportions higher than 5%.

Then, we used the SCTransform function in the Seurat package to normalize the expression matrix of each Seurat object for each brain section separately. For the continuous sections of the whole mouse brain, we grouped the brain section data based on the interval from the appearance to the disappearance of major brain regions in the brain section (e.g. the 123 brain sections of mouse #1 were divided into 12 compartments). We then merged the Seurat objects of brain sections in each group separately. We then used the RunPCA function to perform dimensionality reduction on the merged Seurat objects and performed unsupervised spatial clustering with the spatialCluster function of BayesSpace (parameters:platform="ST", init.method="mclust", model="t", gamma=2,nrep=1000, burn.in=100). Resulting clusters were annotated based on their transcriptomic marker genes identified by the FindAllMarker function of Seurat using default parameters. For each compartment, we first annotated each cluster with broad brain regions, such as olfactory area, cortex, thalamus, hypothalamus, hippocampal region, midbrain, cerebellum, and hindbrain. We then grouped brain sections with the same annotation together and repeated spatial clustering procedure and annotated the second round of cluster results into fine brain regions. We repeated the spatial clustering and annotation process to generate high granularity of brain region parcellation.

Annotations were further verified and compared with ABA (http://mouse.brain-map.org/). Color palette for spatial visualization of clustering and annotation results was optimized using Spaco.[104,111]

Image registration and anatomy-based parcellation

The expression matrix of each section was used to generate total RNA images. The ssDNA and DAPI channel images scanned by ZEISS Z1 were spliced to extract the check lines, which were then registered with the corresponding check lines on the total RNA image so that the total RNA image, ssDNA image and DAPI channel image were aligned in the same coordinate system. Next, we identified the tilt angle and position corresponding to each section on the Allen 3D standard brain atlas. Marker points were then selected to perform cortical registration between the total RNA data and the standard brain atlas. Homemade CellPlot software was used to obtain parcellation of all cortical regions and subregions.

3D reconstruction of coronal sections

2D sections registration: The reconstructed brain sections are registered into the ABA CCFV3. Initially, we use 3D slicer software to manually add corresponding landmark points between the fixed and moving images based on the morphological characteristics of specific brain regions. During this process, we monitored in real-time the overlay effect of the fixed image and the moving image, adjusting the position of the landmark points to align the moving image with the fixed image as closely as possible. After registration, we obtained the transformation matrix of the brain sections. Subsequently, this transformation matrix was applied to the reconstructed cellular and genetic data in the brain, achieving the unified transformation of the data into the CCFv3 framework.

Sample preparation for single-nucleus sequencing

Mouse was anesthetic with the mixture of Loratadine Tablets (50 mg/kg) and Xylazine Hydrochloride (0.1 mg/kg), and perfused with ice-cold artificial cerebral spinal fluid (ACSF) containing (in mM) NaCl 126, KCl 2.5, NaH_2PO_4 1.25, $MgCl_2$ 2, $CaCl_2$ 2, $NaHCO_3$ 26, and glucose 10 (300-305 mOsm). The mouse brain was quickly dissected and transferred to the dish (diameter: 6 cm) that contained bubbled ice-cold ACSF. Then, the brain was divided into two parts along the coronal axis, the dividing site dependent on the tissue that we need to correct. After that, the part that we needed was attached to the platform of the cutting system (Leica VT1200S) and the platform was attached to the cutting chamber which was filled with bubbled ice-cold ACSF. Coronal slices (500 μm) were prepared at the speed of 0.2 mm/s with blade vibration amplitude of 0.8 mm. After the section, brain slices were immediately transferred to the dissection chamber (containing bubbled ice-cold ACSF). Then, target brain areas were carefully dissected according to the

allen-atlas and collected to responding tubes that stored on the dry-ice. After the collection of all brain areas of the mouse, tubes were put into the liquid nitrogen for 3 min and then transferred into the dry-ice. The duration should be less than 10 min from the time point of perfusion to that of put tubes into liquid nitrogen. After the daily collection of all tissues, the boxes that contain dry-ice and tubes were stored in the -80°C refrigerator before being sent out for sequencing.

Single-nucleus suspension preparation

Similar to previously described,[112] frozen brain tissues were rapidly transferred to a 1-ml Dounce homogenizer (TIANDZ) and immediately homogenized in a 1-ml homogenization buffer. After filtered with a cell strainer into a 1.5-ml tube (Eppendorf), solution in the tube was subsequently centrifuged at 500 g for 5 min at 4°C to pellet the nuclei. Then, the pelleted nuclei were diluted in a resuspension buffer at 1000 nuclei/μl for library preparation.

Single-nucleus library preparation and sequencing

Single-nucleus RNA sequencing libraries were prepared using DNBelab C Series High-throughput Single-Cell RNA Library Preparation Kit (MGI, #940-000047-00). In brief, single-nucleus suspensions were processed as follows: droplet generation, emulsion breakage, beads collection, reverse transcription and cDNA amplification to generate barcode libraries. Indexed libraries were prepared according to the manufacturer's protocol (MGI, 1000021082). Qubit ssDNA Assay Kit (Thermo Fisher Scientific, Q10212) was used to quantify the constructed libraries. The library was sequenced on DNBSEQ™ T1 or DNBSEQ™ T7 sequencer with following read length: 41-bp length for read 1, 100-bp read length for read 2 and 10-bp read length for sample index.

Single-nucleus raw data processing

Raw sequencing reads were processed with filtering, demultiplexing barcode processing and 3' UMI counting using the DNBelabC Series HT scRNA analysis Software Suite (v1.0.0) set with default parameters (https://github.com/MGI-tech-bioinformatics/DNBelab_C_Series_HT_scRNA-analysis-software/tree/version1.0). PISA software (https://github.com/shiquan/PISA) was applied to parse raw reads into FASTQ format according to library structure and cell barcode information. Processed reads were then aligned to GRCm38.p3 (mm10) mouse genome with STAR (v2.7.4a) and sorted by sambamba (v0.7.0). Due to the large amount of unspliced pre-mRNA in mouse brain cell nucleus, a custom 'pre-mRNA' reference was created for alignment of count reads to exons as well as to introns. Accordingly, each gene's transcript in snRNA-seq was counted by exon and intron reads together. Finally, a nucleus-gene metric was generated, which was then adjusted by SoupX (v1.5.21) to reduce ambient RNA noise.

Single-nucleus data filtering

In all single-nucleus sequencing libraries, we removed libraries with median gene count $\leq$ 800 and selected the remaining 136 libraries as high-quality libraries. Nuclei were further filtered based on criteria including median gene count > 800, mitochondrial gene content < 5%, and a ratio of UMI counts to gene counts > 1.2. The expression data were then subjected to SCTransform normalization in the Seurat package (v4.3.0). We performed unsupervised clustering on the normalized data using the FindNeighbors and FindClusters functions (parameters: dims = 1:50). Based on the marker genes of each group, the clustering results were divided into six major cell classes: *Neurons*, *Astrocytes*, *Oligodendrocytes*, *Microglia*, *Ventricular cells*, and *Vascular cells*. Nuclei that could not be clearly classified into these six major types were classified as *Uncertain*.

When dividing nuclei into major classes, it was found that some nuclei existed at the boundaries between classes and were classified as the uncertain class without clear marker genes. Therefore, we trained a random forest model to predict the major nuclei classes in order to remove the uncertain nuclei. First, we downsampled each nuclei class and extracted 5,000 nuclei (up to 80% of the type) as the training set. The FindAllMarkers function in the Seurat package was used to identify marker genes for each class in the training set, and further filtered genes with corrected *p* values (p_val_adj) < 0.01 and average $\log_2$ fold change (avg_$\log_2$FC) > 1 as feature genes for the random forest model. Using the SCTransform normalized values as gene-expression data, the randomForest function in the randomForest package (v4.7.1.1) was used to build the model based on the training set (parameter: ntree = 500). Then, the predict function was used to apply the trained model to all single-nucleus data. The model evaluated the probability of the major classes for each nucleus, and we assigned each nucleus to the class with the highest probability. Nuclei with highest probability < 0.9 were discarded. After the iterative clustering and annotation that introduced below, clusters with unclear marker expression were removed. 378,287 nuclei were kept after all filtering processes and used in further analysis.

Single-nucleus iterative clustering and classification

The single nucleus data was first normalized using SCTransform and reduced the dimension using RunPCA. We used the modified RunHarmony function in the harmony package (v0.1.0) to integrate data from different batches. We modified the kmeans clustering algorithm used in the package by adding a new parameter kmeans.algorithm, which replaces the default Hartigan-Wong algorithm with the Lloyd algorithm. We also added two parameters, kmeans.iter.max and kmeans.nstart, to make it applicable to larger datasets (parameters: assay.use ="SCT", reduction = "pca", dims.use = 1:50, theta = 2, max.iter.harmony = 10, max.iter.cluster = 20, kmeans.algorithm = "Lloyd", kmeans.iter.max = 1000, kmeans.nstart = 20, epsilon.cluster = -Inf, epsilon.harmony = -Inf).

To further subdivide cell types, we followed the iterative clustering method for single-cell sequencing data in the scrattch.hicat package (https://github.com/AllenInstitute/scrattch.hicat), while using the batch correction method in harmony to correct the batch

effects in different batches during each iteration. This allowed us to reduce batch effects while clustering cell clusters in as much detail as possible. The specific steps are shown as follows:

(1) First, we defined a clustering function, OnestepCluster, which takes the single cell data in Seurat object format and performs SCTransform normalization, RunPCA dimension reduction, and RunHarmony batch correction. The clustering results are checked using the MergeCluster function in step (2) to merge the clusters without distinguishable gene expression differences.
(2) The MergeCluster function calculates the Pearson correlation coefficient between any two clusters. Clusters with fewer than 20 cells will be merged directly with the other cluster with the highest Pearson correlation coefficient, and then the Pearson correlation coefficient is recalculated for all clusters. Next, we calculated the gene expression differences between the cluster and the other top 3 clusters with the highest Pearson correlation coefficient. The FindMarkers function is used to calculate the differentially expressed genes G between any two clusters. To shorten the computation time, each cluster is downsampled to 500 cells for calculation. The differential gene score S is calculated based on the following formula:

$$S = \sum_{G} min(-log_{10}(P_{adj}), 20)$$

Among them, differentially expressed gene G requires corrected p values < 0.01 and average fold change > 1, with at least 50% of cells expressing the gene in the highly expressed cluster, and the expression proportion of the gene in the lowly expressed cluster is more than 50% lower than the highly expressed clusters. If the number of differentially expressed genes G is less than 5 or the differential gene score S is less than 200, the two clusters will be merged. All calculations will be repeated until the differential gene score S between any two clusters larger than 200.

(3) We defined the clustering recursive function IterCluster, which combines the OnestepCluster and MergeCluster in step (1-2). If all clusters are merged in the result, the recursion will be terminated because it cannot be further split. If there are more than one clusters in the result, the clusters with more than 50 cells are selected and the IterCluster function is performed on this cluster again. The process continues until all clusters cannot be further splitted, and all clustering results are summarized and returned.

At the beginning, we used the results of the six major nuclei classes as the start point. For each major class, the IterCluster recursive function is executed, and eventually, all clusters splitting results are returned. We annotated the clusters based on the marker genes, and removed some groups with unclear marker genes. In the end, we obtained 308 clusters covering 378,287 high quality nuclei.

Single-nucleus cluster dendrogram construction

Dendrogram of 308 nuclei clusters was constructed based on the marker gene expression. First, the FindAllMarkers function in Seurat software package was used to identify marker genes for all cell types. Only genes with adjusted p values (p_val_adj) < 0.05 and avg_log$_2$FC > 0 were kept. For each nuclei cluster, the top 20 genes with the largest avg_log$_2$FC were selected. Marker genes with expression in less than 20% of nuclei in the corresponding cluster were filtered out. Next, the mouse whole-brain snRNA-seq data were divided into two groups: neuronal and non-neuronal nuclei. For each group, the AverageExpression function was used to calculate the average expression values of marker genes for each nuclei cluster. The pvclust function in the pvclust package (v2.2.0) was used to construct a classification dendrogram, based on the Spearman correlation distances between clusters. Finally, the merge function was used to combine two dendrograms together.

Independence test of nuclei clusters

We tested the independence of each cluster in the iterative clustering results to ensure there are sufficient differences between nuclei clusters. We used the randomForest function in the randomForest package to build a random forest model for all 308 clusters. We first used the FindAllMarkers function in the Seurat package to find the marker genes for each cluster, Only the genes with an adjusted p value (p_val_adj) < 0.05 and an avg_log$_2$FC > 0. For each nuclei cluster, we selected the top 50 genes with the highest avg_log$_2$FC and used them as the feature genes for the random forest model. Then, the single-nucleus data was downsampled, and 200 nuclei were selected for each nuclei cluster. Using the SCTransform-normalized values as expression data, we built the random forest model using the randomForest function (parameters: ntree = 1000). The confusion matrix was calculated using the out-of-bag (OOB) data of the model, Prediction accuracy of the confusion matrix data was used as the standard for evaluating independence clusters.

Single-nucleus data co-clustering with published dataset

We used two public scRNA-seq datasets as references. One of which is the mouse whole nervous system scRNA-seq dataset,[3] we removed cell types from the spinal cord and peripheral nervous system since these cells were not included in our snRNA-seq dataset. For the other public dataset,[28] which only contains single-cell data from the cortex and hippocampus structures, we extracted cell types belonging to these two regions from our dataset and discarded clusters with cell counts < 20 for comparison purposes.

Please cite this article in press as: Han et al., Single-cell spatial transcriptomic atlas of the whole mouse brain, Neuron (2025), https://doi.org/10.1016/j.neuron.2025.02.015

We first downsampled 200 cells for each cell type in each dataset separately. Using the SCTransform function in the Seurat package (v4.3.0), we normalized each dataset (parameters: variable.features.n = 5000, method = "glmGamPoi") and reduced the data using the RunPCA and RunUMAP functions (parameters: dims = 1:50). We used the FindAllMarkers function to find marker genes for each cell type and only kept genes with a corrected p value (p_val_adj) < 0.05 and an avg_log$_2$FC > 0. We then summarized the top 50 genes with the highest avg_log$_2$FC for each cell type as the marker gene set for that dataset. Using the FindIntegrationAnchors and IntegrateData functions, we integrated our dataset with any one of the publicly available datasets, using the intersection of marker gene sets as integration anchors. We then reduced the integrated data again using RunPCA and RunUMAP (parameters: dims = 1:100), and performed clustering using FindNeighbors (parameters: reduction = "pca", dims = 1:100) and FindClusters (parameters: resolution = 3, n.start = 10, algorithm = 1).

For the integrated clustering results, we calculated the proportion R of a cell type x in our dataset that clusters with a cell type y in other public dataset using the following formula:

$$R = \sum_{i}^{C} min(R_{ix}, R_{iy})$$

where C represents all clusters generated after re-clustering the integrated dataset, i represents any cluster in C, Rix represents the proportion of cell type x in cluster i among all cell types of x, and Riy represents the proportion of cell type y in cluster i among all cell types of y.

Stereo-seq cell type transfer

Due to the intricate diversity of neuron types throughout the entire brain and the wide-ranging spatial transcriptomic regions, we partitioned both the snRNA-seq data and Stereo-seq data into six distinct, mutually independent regions (cerebral cortex, cerebral nuclei, interbrain, midbrain, hindbrain, cerebellum). When transferring cell types to a specific region within the Stereo-seq data, we selected the snRNA-seq neuron clusters from the corresponding region as the reference set. Clusters comprising less than 20 nuclei were excluded. Considering that non-neuronal cells exhibit relatively lower regional selectivity in their distribution across the entire brain, we utilized all non-neuronal cells from the complete mouse brain snRNA-seq dataset as the reference set. Each region in Stereo-seq data was transferred using the corresponding neuronal and all non-neuronal cell clusters. In addition, the Stereo-seq data also included fiber tracks and ventricular regions, which are not primary structural regions of the mouse brain and predominantly comprise non-neuronal cells. Consequently, for these regions, we exclusively employed non-neuronal cells as the reference set for cell type prediction. We defined the cells with more than 100 genes and the percentage of mitochondrial genes less than 15%. Prior to cell type transfer, each cell cluster in the snRNA-seq data was downsampled to 1000 nuclei. We computed the marker genes for each cluster, selecting the top 300 genes (sorted by fold changes, excluding genes associated with mitochondria or ribosomes), which were subsequently utilized in the subsequent training phase.

We used Spatial-ID, a novel cell type mapping algorithm,[29] to annotate single cells in Stereo-seq data with cell types classified by snRNA-seq analysis. To remove uncertainty annotation caused by bubble artifacts in Stereo-seq data, cells in Stereo-seq data with detected genes less than 100 and percentage of mitochondrial genes larger than 15% were removed in the transfer process (Figure S3). This filtering process resulted in the exclusion of 20,019 cells. The remaining 4,209,604 cells were assigned as high-quality cells and used for cell type annotation. The annotation procedure mainly consisted of two stages. In the first stage, we trained a four-layer deep neural network (DNN) with the snRNA-seq data. The DNN model included two hidden layers of 2048 and 1024 nodes and was trained by a Cross Entropy loss with learning rate = 3×10^{-4}, weight decay = 1×10^{-6}. The trained DNN predicted the initial probabilities of defined cell types for single cells on the Stereo-seq data. In the second stage, we applied a graph convolution network (GCN) including two autoencoders and a classifier to integrate gene expression, spatial neighborhood information and cell type instruction generated in the previous stage to refine the probabilities. Spatial neighborhood information of the Stereo-seq data was encapsulated into an adjacency matrix of cells with normalized Euclidean distances as values for non-zero elements. The GCN model took the gene expression matrix, the distance-weighted adjacency matrix and the initial probabilities as inputs and produced the final probabilities after 200 epochs of training with learning rate = 1×10^{-2}, weight decay = 1×10^{-4}. The two autoencoders of the GCN model were trained via a self-supervised learning strategy with reconstruction losses and the classifier was trained by a Cross Entropy loss. Spatial-ID used in this study was implemented with PyTorch (v1.13.1) and PyTorch Geometric (v2.1.0) packages in Python (v3.8.10).

Evaluation of cell type transfer consistency and accuracy

To evaluate the consistency of Stereo-seq data and the impact of different quality control criteria on cell type annotation, we applied a series of cell quality cutoffs (ranging from 100 to 400 MID counts per cell). Stereo-seq data were processed separately for each cutoff to annotate cell types. Consistency rates were calculated for each comparison between different cutoffs. The results showed that Spatial-ID transfer of cell clusters maintained over 80% consistency across filtering thresholds, demonstrating the robustness of cell cluster transfer (Figures S3C and S3D). To assess the accuracy of Spatial-ID, we calculated the scaled Pearson correlation of gene expression between cell types annotated in Stereo-seq sections and snRNA-seq data. For cell clusters, the Pearson correlation was scaled within each cell subclass (Figures S3E and S3F).

Please cite this article in press as: Han et al., Single-cell spatial transcriptomic atlas of the whole mouse brain, Neuron (2025), https://doi.org/10.1016/j.neuron.2025.02.015

Analysis of cell type distribution across brain regions

We calculated the density distribution of cell clusters across brain regions using Stereo-seq sections. Density was derived by dividing the count of a specific cell cluster within each region by the region's area. The regions' areas were computed by tracing lines using total RNA and registered ssDNA images of the coronal sections.

Cell ratio of a cell cluster is derived by dividing the count of the cell cluster within each region by the total cell count of the region. The "relative max cell ratio" (used in Figure S7A) was defined as follows:

$$Relative\ max\ cell\ ratio = \frac{R_{most} - R_{sec}}{R_{most}}$$

where R_{most} represents the cell ratio of the cluster in the most populous area; R_{sec} represents the cell ratio of the cluster in the second most populous area.

Regulon analysis

The regulon activity analysis of transcript factors was performed using standard pySCENIC pipeline.[113] Transcriptomic profiles of previously divided bins (bin100) were used as input. The GENIE3 algorithm[114] was used to reconstruct the co-expressed gene network for each transcript factor. This network was then analyzed and filtered according to cisTarget database (https://resources.aertslab.org/cistarget/), resulting in regulons consisting of each TF and its potential targets. The activity of a regulon within each bin was calculated by AUCell using default parameters and threshold, and then mapped to physical space for visualization. We aggregated potential target genes sharing the same TF across different developmental time points by using the *union* function. Aggregated regulons were subjected to AUCell again to re-calculate comparable activity scores across each developmental stage. The regulon activity of each anatomic region was defined as the mean activity of all bins belonging to the region.

Identification of spatial gene modules

Spatially co-expressed genes and co-activated regulons are identified and grouped into modules using Hotspot.[45] Top 5000 highly variable genes or all identified regulons were used as input. Gene expression in each bin100 was scaled by size factor and log transformed. Then the spatial autocorrelation score was calculated using *compute_autocorrelations* function. Significantly auto-correlated genes or regulons with *p* value less than 0.05 were kept and further grouped into modules using the *create_modules* function with min_gene_threshold = 10 and fdr_threshold = 0.05 (for the regulon: min_gene_threshold = 5, C > 0.15 and fdr_threshold = 0.05, for genes in developmental sections: min_gene_threshold = 20 and fdr_threshold = 0.05). Identified gene or regulon clusters were annotated to related anatomic brain regions according to their spatial localization and contents of genes or TFs.

We identified gene modules with spatial selectivity through gene module enrichment analysis of 123 brain sections from mouse #1. To identify gene modules with regional selectivity among these modules, we calculated the enrichment scores of gene modules in bin100 spots from different brain regions of each brain section. For a given gene module in a particular brain section, we calculated the significance of the difference in gene module enrichment scores for bin100 spots across brain regions. If the enrichment score of a gene module in a specific brain region was significantly higher than that in other brain regions (p_val_adj < 0.01), we considered this gene module to be region-specific for that brain region. Due to the fact that computer-based methods cannot accurately annotate gene modules that cover multiple brain regions, we combined computational and manual methods to determine the brain region selectivity of each gene module and annotate the gene modules.

Gene ontology analysis and enrichment scoring

Gene ontology (GO) analysis was performed on identified modules using clusterProfiler.[105] Gene members of each gene module were used as input. For TF regulon clusters, corresponding TFs and top 10 target genes of each regulon member were used. GO enrichment score and significance for biological process (BP), Molecular Function (MF) and Cellular Component (CC) were calculated with the compareCluster function using the *org.Mm.eg.db* database with default parameters. BP, MF, CC with Benjamini-Hochberg-adjusted *p* values less than 0.05 were considered to be enriched in corresponding modules. For manually chosen developmental related process, we extracted the gene sets from Mouse Genome Informatics website (http://www.informatics.jax.org/vocab/gene_ontology), and calculated enrichment scores for these gene set within each bin100, using the AddModuleScore function in Seurat[94] package. The results were then visualized in groups by brain sections, using the ggplot2 package.

Spatial expression pattern analysis

To quantify and analyze the spatial distribution of transcriptomic features, cortex region of each developmental mouse brain section was digitized and divided into conformal layers or columns along the dorsal-ventral and rostral-caudal axis using the Spateo package digitization pipeline.[57] Concretely, for each brain section, cortex-corresponding clusters were subjected to the extract_cluster_contours function, and converted into a closed contour line indicating the boundary of cortex region. We arbitrarily divided and labeled the boundary of cortex into 4 segments, indicating the dorsal, ventral, rostral and caudal side of cortex, respectively, which were further used by digitize function to generate relative dorsal-ventral and rostral-caudal coordinates for each bin100 within cortex. We then performed differential analysis on gene expression or regulon activities distribution along the dorsal-ventral axis to identify laminar peak shifting in the developmental process as described in Figure 5F. Generalized linear models are applied on expression

distribution of the rostral-caudal axis to detect significant gradient patterns, using the glm_degs function in Dynamo package[115] with default parameters. Genes with Benjamini-Hochberg-adjusted *p* values greater than 0.05 or expressed in less than 25 percent of bins in cortex were filtered out. Then, min-max normalized expressions of each significant gradient gene were further fitted using sklearn.linear_model. LinearRegression[116] to get a normalized gradient coefficient and a coefficient of determination, where genes with coefficient of determination greater than 0.05 were shown in Figures 5G and S13D.

Identification of region-enriched genes

For identification of region-enriched genes, the gene density of each region was calculated as nCounts/region size, then the fold change was calculated as the highest region density/median density of all regions. Region-enriched genes were defined as fold change > 1.5 and density > 25 per mm^2. Finally, some genes were added or deleted based on manual screening by checking expression images of individual genes obtained by spatial transcriptomic experiment. Layer enriched genes were calculated similarly except the cortex was manually divided into layer 1-6.

Identification of convergent and divergent gene pairs

The lncRNAs we used here were derived from the gene annotation of Ensembl V93.[117] Long non-coding RNA (lncRNA) is defined as a non-coding gene/transcript larger than 200bp in length according to the definition from Ensembl (https://www.ensembl.org/info/genome/genebuild/biotypes.html). We divided lncRNA-mRNA gene pairs into divergent and convergent groups based on the distance between the transcription start sites of lncRNA and mRNA on the genome. In a gene pair, lncRNA and mRNA are close or overlap and need to be on different DNA strands. When the transcription start site (TSS) distance between lncRNA and mRNA is greater than -1000 nt and less than 10000 nt, we define it as a divergent gene pair (TSS distance = TSS in plus strand – TSS in minus strand). When the TSS distance between lncRNA and mRNA is less than -1000 nt and lncRNA overlaps with mRNA, we define it as a convergent gene pair.

Calculation of lncRNA-mRNA gene pairs

To calculate the correlation of lncRNA-mRNA expression in different brain regions of mice, we combined the gene expression levels in the same brain region, and then calculated the CPM value of each gene in each section. Then filter out low expression values (lncRNA + mRNA >1), and calculate the lncRNA-mRNA Pearson correlation coefficient.

To calculate the differential expression of lncRNA-mRNA in different cell types, we calculated the average expression of each gene in different cell types. Then calculated the fold change and adjusted *P*-values (p_val_adj) of lncRNA and mRNA in the two cell types (FC = $\log_2$ (lncRNA/mRNA)). When the adjusted *P*-values (p_val_adj) were less than 0.01, the absolute values of fold changes (FCs) were greater than 1, and the signs of FCs in the two cell types were opposite, we consider that lncRNA and mRNA were antagonistic expressed in these two cell types.

QUANTIFICATION AND STATISTICAL ANALYSIS

No statistical methods were used to predetermine sample sizes, but the sample sizes here are similar to those reported in previous publications. No randomization was used during data collection as there was a single experimental condition for all acquired data. Data collection and analyses were not performed blind to the conditions of the experiments as all experiments followed the same experimental condition. Statistical details of experiments and analyses can be found in the figure legends and main text above.

ADDITIONAL RESOURCES

An interactive website for visualizing gene expression patterns and cell type distributions in the mouse brain (https://mouse.digital-brain.cn/spatial-omics).